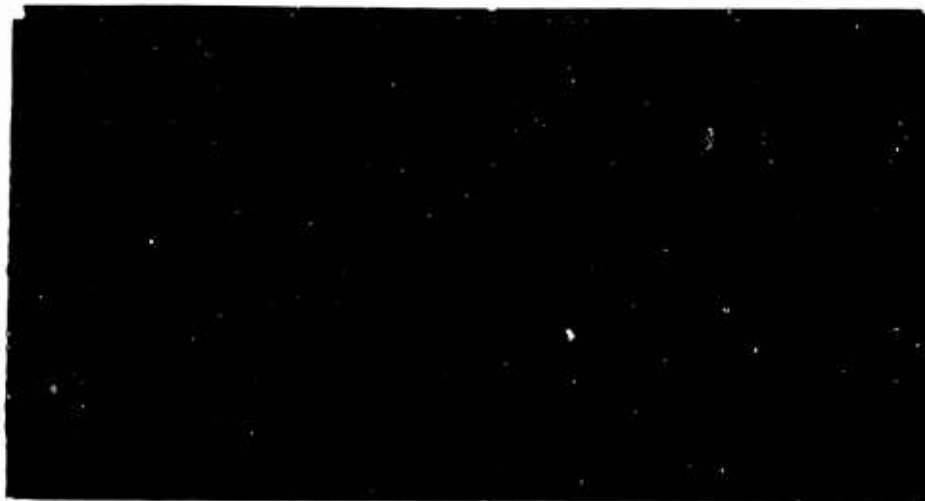


AD 608684

COPY	1	OF	1	mm
HARD COPY	\$. 2.00 1.00			
MICROFICHE	\$.0.50			

48p



DDC
RECEIVED
DEC 5 1964
DDC-IRA B

Sandia Corporation

Contractor for U.S. Atomic Energy Commission
ALBUQUERQUE, NEW MEXICO LIVERMORE, CALIFORNIA

ARCHIVE COPY

**Best
Available
Copy**

SC-RR-64-979

THE HYPERSONIC PLASMA CONVERTER: II

K. J. Touryan, 7421-1
Sandia Laboratory, Albuquerque

November 1964

ABSTRACT

As a continuation to Part I of the hypersonic plasma generator known as ASP (Aerodynamic Supply of Power), experimental analyses have been extended to investigate in detail the various parameters that govern the operation of the generator. A final feasibility study was made, and possible modifications to the theory are outlined. Test runs in the Sandia Corporation arc jet with air as the working fluid at 12,000 BTU/lb have generated 8 amp/in² short circuit currents and 2.3 volts open circuit voltage. Under favorable conditions, full-size re-entry vehicles in the altitude range of 200,000 to 80,000 feet are expected to yield several kilowatts of power.

* Published as SC-4960(RR), date January 1964.

ACKNOWLEDGMENTS

The author is indebted to P. T. Lubeck for his help collecting and reducing the data and supplying the arc jet operation characteristics. Special thanks are extended to Messrs. G. M. Baker and J. V. Williams for operating the plasma jet, and to Mr. W. Haskell for designing and procuring the models. Dr. W. Byatt and Captain G. E. Weinstein, of the University of New Mexico, helped in the initial stages of the ASP generator development.

Issued by Sandia Corporation,
a prime contractor to the
United States Atomic Energy Commission

LEGAL NOTICE

This report was prepared as an account of Government sponsored work. Neither the United States, nor the Commission, nor any person acting on behalf of the Commission:

A. Makes any warranty or representation, expressed or implied, with respect to the accuracy, completeness, or usefulness of the information contained in this report, or that the use of any information, apparatus, method, or process disclosed in this report may not infringe privately owned rights, or

B. Assumes any liabilities with respect to the use of, or for damages resulting from the use of any information, apparatus, method, or process disclosed in this report.

As used in the above, "person acting on behalf of the Commission" includes any employee or contractor of the Commission, or employee of such contractor, to the extent that such employee or contractor of the Commission, or employee of such contractor prepares, disseminates, or provides access to, any information pursuant to his employment or contract with the Commission, or his employment with such contractor.

Printed in USA. Price \$1.00. Available from the Office of
Technical Services, Department of Commerce
Washington 25, D. C.

TABLE OF CONTENTS

	<u>Page</u>
List of Symbols	6
Introduction	9
Theory	10
Experiments	11
A. Test Conditions	11
B. Parameters Influencing Generator Output	20
C. Experimental Results	21
D. Optimum Results	30
Free Flight Conditions	36
Future Work	36
Appendix	41
List of References	47

LIST OF TABLES

Tables

I	Electron Density in Argon Gas	18
II	Electron Density in Air	19
III	Model Dimensions	22
IV	Open-Circuit Voltage	23
V	Output with and without Seeding	25
VI	Model Materials	30
VII	Optimum Output per Emitter Area	34

LIST OF ILLUSTRATIONS

Figure		Page
Frontispiece	A Hypersonic Plasma Generator	8
1	Schematic of ASP Generator	9
2	Sketches of ASP Plasma Jet Models	12
3	Surface Pressure on S-6 Model in 160 kw Jet (Argon)	13
4	Kinetic Temperature Near Body of S-6 Model in 160 kw Jet (Argon)	14
5	Surface Pressure on S-6 Model in 160 kw Jet (Air)	15
6	Surface Pressure on S-6 Model in 160 kw Jet (Air, Nose Cone Section Enlarged)	16
7	Kinetic Temperature Near Body Surface of S-6 Model in 160 kw Jet (Air)	17
8	Short-Circuit Current Versus Emitter Area for Two Values of Effective β . Runs Made in Argon Gas with 5000 BTU/lb Energy, and Nitrogen at 12,000 BTU/lb	20
9	Output from Geometrically Similar Models with Different Emitter Areas	22
10	Power Output for Various Model Geometries at Constant Jet Energy	24
11	Degree of Ionization on Short Circuit Current Output. Argon-Nitrogen Mixtures.	26
12	Short Circuit Current versus Electron Density (Unseeded Gas from Spectroscopy, Seeded Gas using Saha Equation)	26
13	Power Output and V-I Characteristics of S-6 Model in Argon, Nitrogen and Air	27
14	Dimensionless Short-Circuit Current versus $1/\beta$ for Various Resistance Parameters C_r in Argon and in Air	29
15	Output Data for $\beta = 0.15$, $V_T = 1$ ev, $\epsilon = 0.1$ from S-6 Tungsten Model in Argon at 5000 BTU/lb	31
16	Power Levels from Various Models Showing the Effect of Argon Gas Energy on Output	31
17	Voltage-Current Characteristics for $V_T = 1.0$, Various β and ϵ Values in Argon Gas	32
18	Effect of Contact Resistance between Pyrolytic Graphite Shell and Carbon Substrate on Output	33
19	Dimensionless Maximum Power versus ϵ for Various Values of β and r .	35
20	Electron Density and Kinetic Temperature Near Stagnation Point for Blunt Re-entry Vehicle at Various Altitudes	37
21	Electrical Conductivity as a Function of Temperature for Equilibrium Air at Various Densities (Equation B-5, Reference 1)	38

LIST OF SYMBOLS

- A_e (or A_{em}) - emitter area
 A_c - collector area
 $C = aRl_{th}/(\sigma V_T)$
 D - diffusion coefficient
 E - emf or electric field (volts)
 e - electronic charge 1.60207×10^{-19} coulombs
 h - Planck's constant
 I - current (amperes)
 $i = I/I_{th}$
 $i_{sc} = I_{sc}/I_{th}$ (short circuit current)
 J, J - current density, amps/in²
 k - Boltzmann constant 1.3709×10^{-16} erg/deg
 L - characteristic length
 m_e, m_i - electronic and ionic mass, respectively
 P - power (watts)
 p - pressure
 R - emitter radius
 r - resistance
 r_p, r_c, r_L - plasma, contact, and load resistance, respectively
 T_e - electron temperature
 T_{em} - emitter surface temperature
 T_c - collector surface temperature
 v - velocity
 V - potential (volts)
 V_{oc} - open circuit potential
 V_T - plasma temperature equivalent potential

LIST OF SYMBOLS (cont)

$V_{T_{em}}$ - emitter temperature equivalent potential

V_{em} - emitter sheath potential

V_c - collector sheath potential

Greek Symbols

α - a fraction in definition of C

$\beta = I_{eem}/I_{ec} \sim A_{em}/A_c$

$\gamma = I_{ic}/I_{ec} \approx 1/155$ for air

$\delta = I_{th}/I_{eem}$

ϵ - dielectric constant

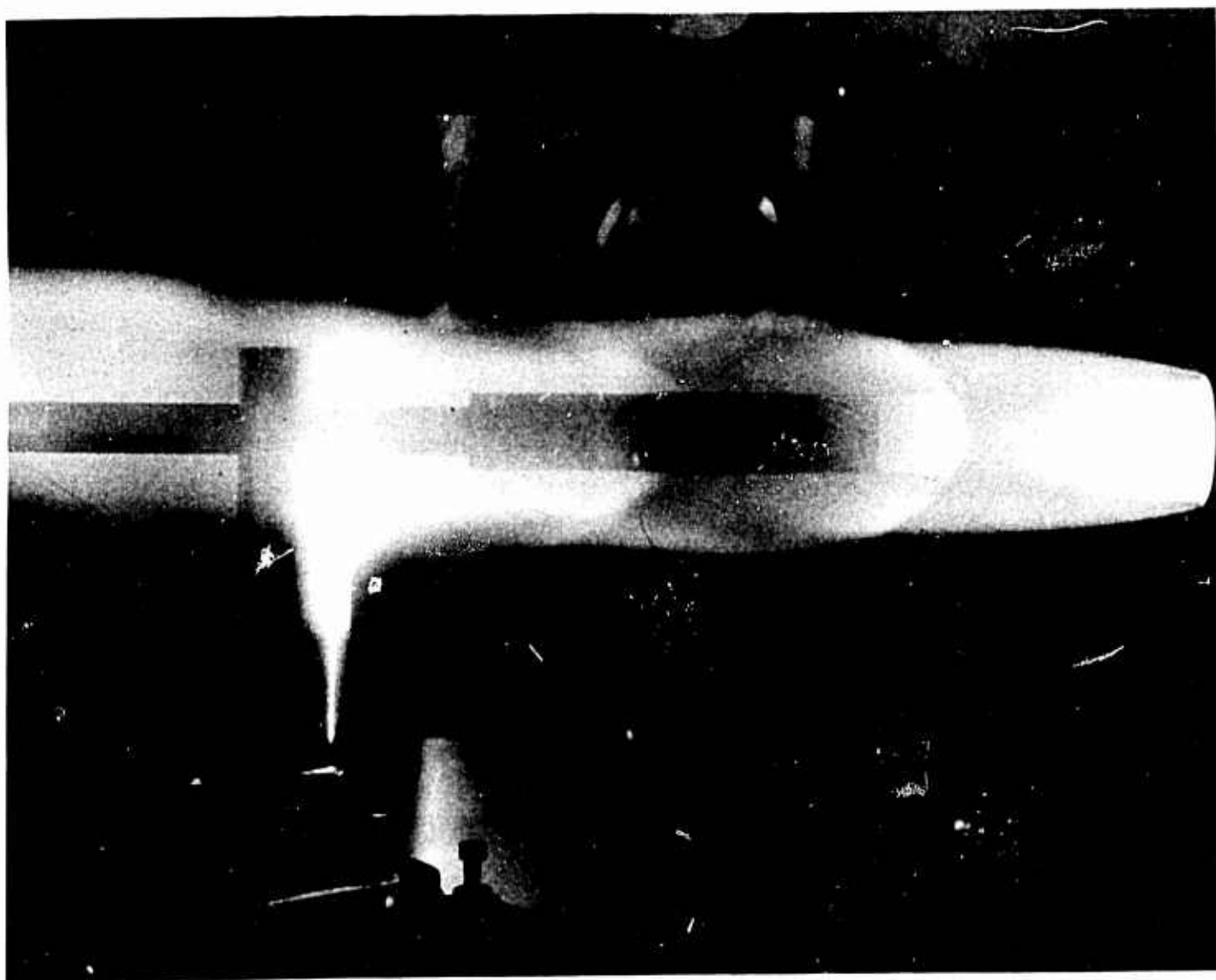
θ - spherical coordinate (in Appendix $\theta = kT_e/e$)

μ - mobility

σ - electrical conductivity mhos/cm

τ - time

$\phi_{e,c}$ - work function (in Appendix B and C, ϕ = potential)



Frontispiece. A Hypersonic Plasma Generator

THE HYPERSONIC PLASMA CONVERTER

Introduction

The operational principle of the hypersonic plasma generator has been discussed in detail in Part I (Reference 1) of this two-part report. Briefly, the nose cone of a re-entry vehicle serves as a thermionic emitter of electrons, or a cathode (see Figure 1). These electrons are then conducted through the shock ionized stream, increased in kinetic energy by collisions, and collected over the relatively cool vehicle afterbody which is electrically insulated from the nose cone and which serves as an anode, or a collector. A load connected between the cathode and the anode within the vehicle completes the circuit. The generator has the basic features of a plasma thermocouple and, for its power output depends primarily on the large temperature and area differences between emitter and collector, with the kinetic energy of the plasma electrons as its energy source.

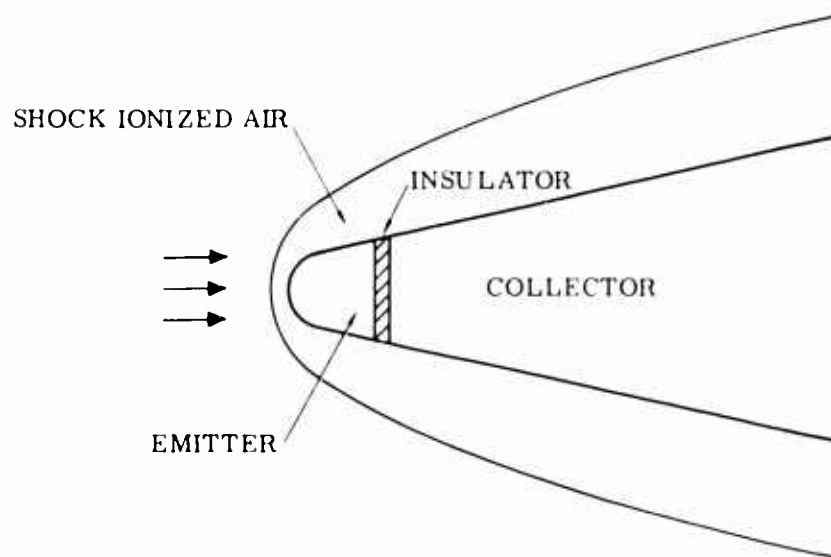


Figure 1. Schematic of ASP Generator

In addition to the several references mentioned in Reference 1, two more works (References 2 and 3) have been published recently which deal with the ASP generator. The first work summarizes the high points of both Reference 1 and the present report. The second work summarizes the progress reports of the work done by the Electrical Engineering Department of the University of New Mexico on a contract with Sandia Corporation starting January 1963 and ending June 1964.

Theory

For a full treatment of the theory of the plasma generator the reader is referred to Reference 1 and several references quoted therein. We repeat briefly the salient points in its development, the space-charge neutralized volt-ampere characteristics ($V_{em} < 0$, V_{em} - emitter sheath potential) of the generator can be represented by Equation 5 from Reference 1, or,

$$V = \left(\frac{kT_e}{e} \right) \ln \left[\frac{I_{ec}}{I_{eem}} \left(\frac{I_{th} + I_{iem} - I}{I_{ic} + I} \right) \right] + (\phi_e - \phi_c) - Ir \quad (1)$$

where

T_e - electron temperature

I_{ec} - random electron current to collector

I_{eem} - random electron current to emitter

I_{th} - thermionic emission current

I_{iem} - random ion current to emitter

I_{ic} - random ion current to collector

ϕ_e, ϕ_c - work functions of emitter and collector respectively

$r(r_p, r_c, r_L)$ - circuit resistance (plasma, contact and load)

The open circuit voltage then becomes

$$V_{oc} = V_T \ln \left[\frac{1}{\beta} \left(\frac{1 + \gamma/\delta}{\gamma/\delta\beta} \right) \right] + \phi_e - \phi_c \quad (2)$$

where, there has been introduced the notation of Waymouth, Reference 4, or

$$\beta = I_{eem}/I_{ec}$$

$$\gamma = I_{ic}/I_{ec}$$

$$\delta = I_{th}/I_{eem}$$

V_T = voltage equivalent of plasma electron temperature

For $V_{em} > 0$ (e. g. $\delta \sim 1$), Equation 2 changes to

$$V_{oc} = V_{Tem} \ln \delta / \gamma + V_t \ln 1/\gamma + \phi_e - \phi_c \quad (3)$$

where V_{Tem} = voltage equivalent of emitter temperature.

The short circuit current, on the other hand, follows by setting $V = \Delta\phi = 0$

$$I_{sc} r = V_T \ln \left[\frac{1 + \gamma/\delta - i_{sc}}{\gamma/\delta + \beta i_{sc}} \right] \quad (4)$$

where i_{sc} - nondimensional current I_{sc}/I_{th} .

For zero resistance, Equation 4 can be simplified to yield (Reference 4)

$$I_{sc} = \frac{I_{th}}{1 + \beta} \quad (5)$$

or, if back emission from the collector I_{th}^c is included

$$I_{sc} = (I_{th} - I_{th}^c \beta) / (1 + \beta) \quad (6)$$

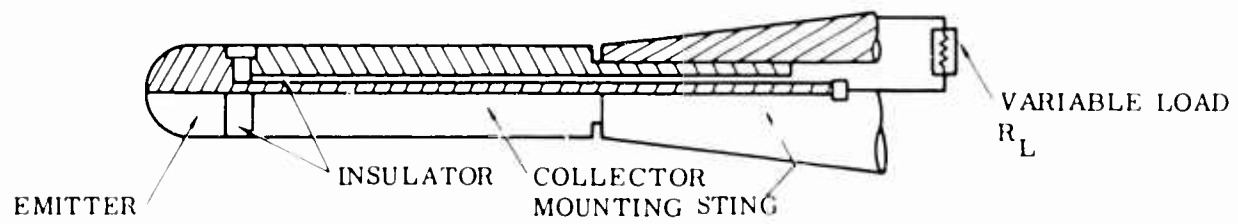
It should be noted that the basic volt-ampere characteristics equation above has been derived on the basis of a rather unrealistic assumption of constant electron temperature around the vehicle and a constant electron density. As will be shown later, the gas temperature in the flow field changes approximately 40 degrees while expanding over a 12-degree hemisphere cone. Electron densities can decrease by as much as three orders of magnitude from emitter to collector. Furthermore, because of large currents (20-30 amps/in²) being dumped in the plasma jet, joule heating and Thompson effects may become prominent in disturbing the plasma temperature distribution. These and other modifications necessary for refining the ASP generator theory are discussed in detail in the Appendix.

Experiments

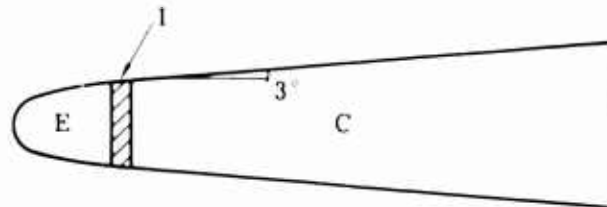
To verify the analytical predictions of the hypersonic generator, an extensive set of experiments were performed in the Sandia Corporation 160 kw plasma arc tunnel. The various model geometries used in the plasma tunnels are shown in Figure 2.

A. Test Conditions

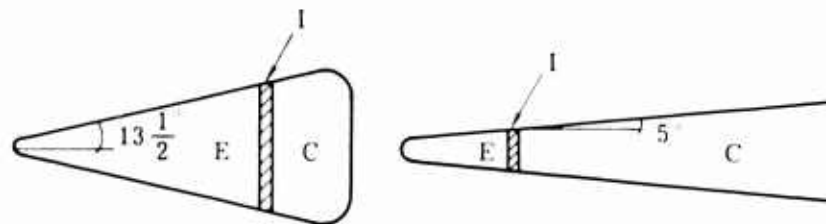
The average diameter of the models and of the plasma jet was 3/4 inch and 1-1/4 inches, respectively. The details of the flow field around an S-6 model in the 160 kw plasma jet, with argon and air as the working gases are presented graphically in Figures 3 through 7 and tabulated in Tables I and II. As observed from this data, the average flow Mach number is 2.5-3.0 with mean energy inputs to the jet of 5000 BTU/lb for argon and 12,000 BTU/lb for air (or nitrogen). The ambient pressure in the test chamber is of the order of 7 mm (0.01 atm) and stagnation pressures range from 0.06 to 0.13 atm. Figure 7 shows the equilibrium and nonequilibrium calculations of the temperature in the jet for air at various energy inputs over a



(a) Model S-0 (Typical Cut-Out)



(b) Model S-6

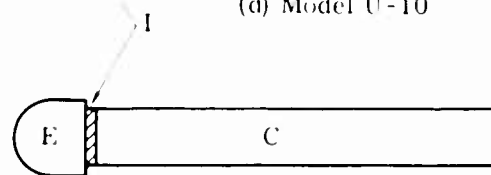


(c) Model S-30

Model S-10



(d) Model U-10



(e) Model U-0

IN ABOVE E = EMITTER C = COLLECTOR I = INSULATOR

Figure 2 Sketches of ASP Plasma Jet Models

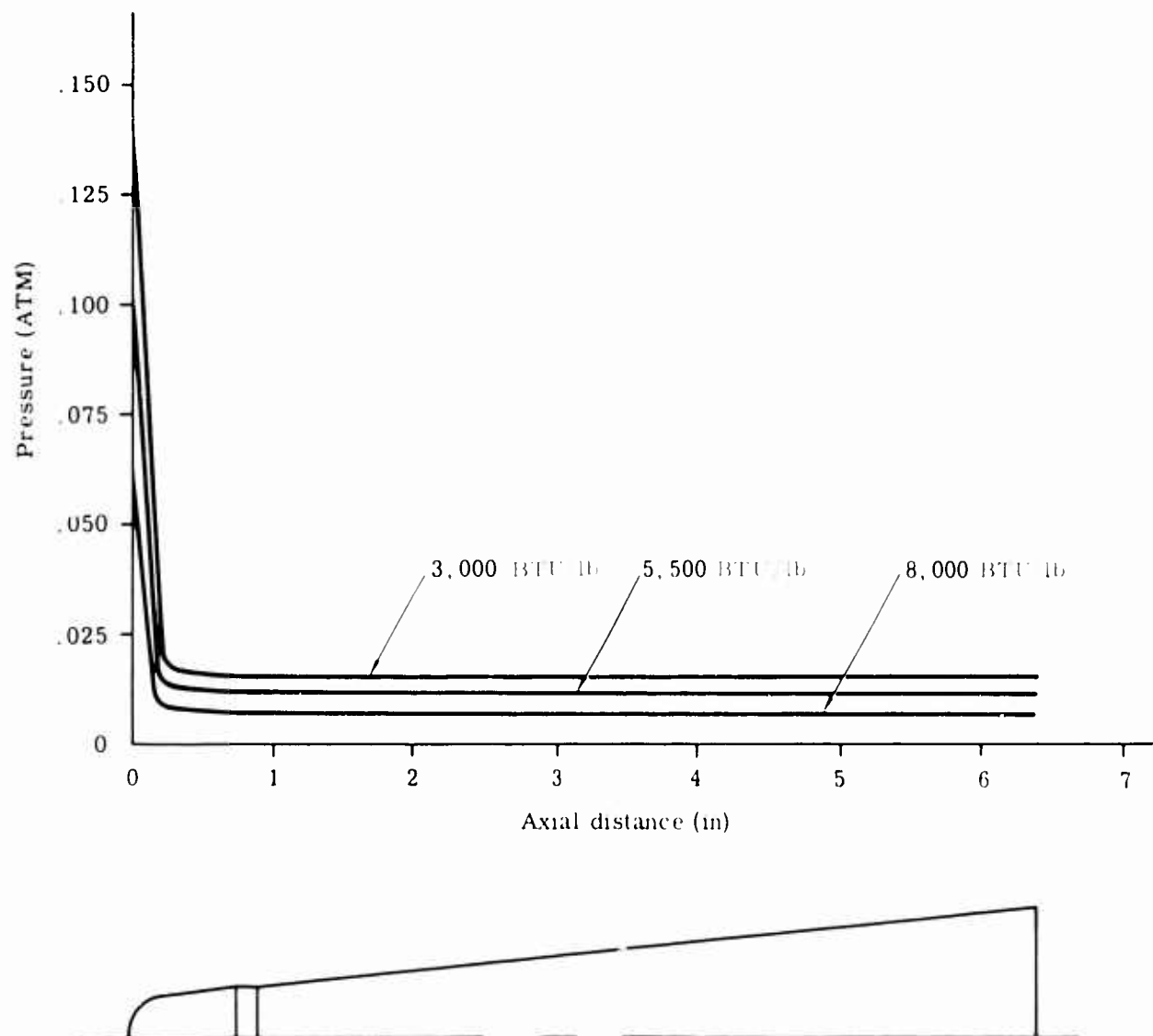


Figure 3. Surface Pressure on S-6 Model in 160 kw Jet (Argon)

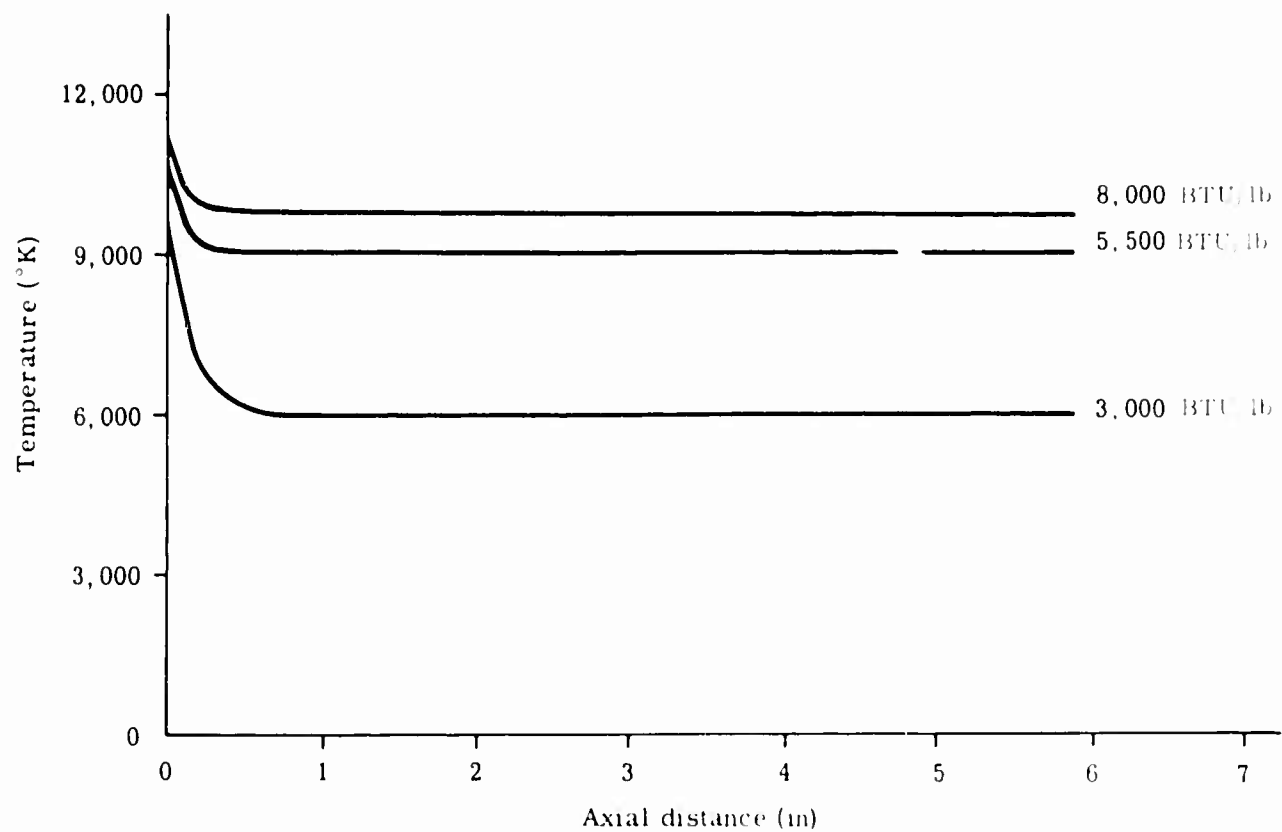


Figure 4. Kinetic Temperature Near Body of Sub Model in 160 kW Jet (Argon)

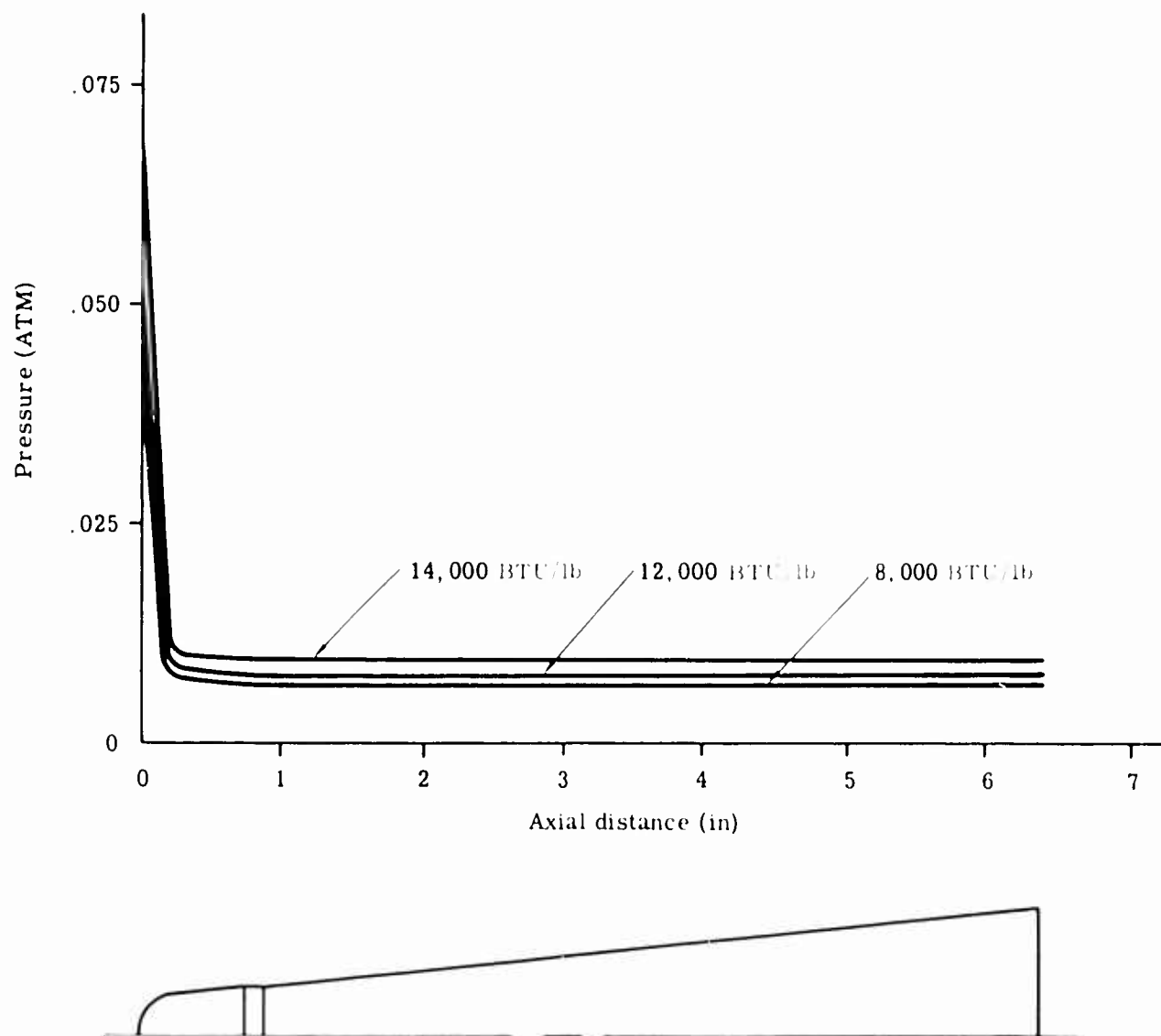


Figure 5. Surface Pressure on S-6 Model in 160 kw Jet (Air)

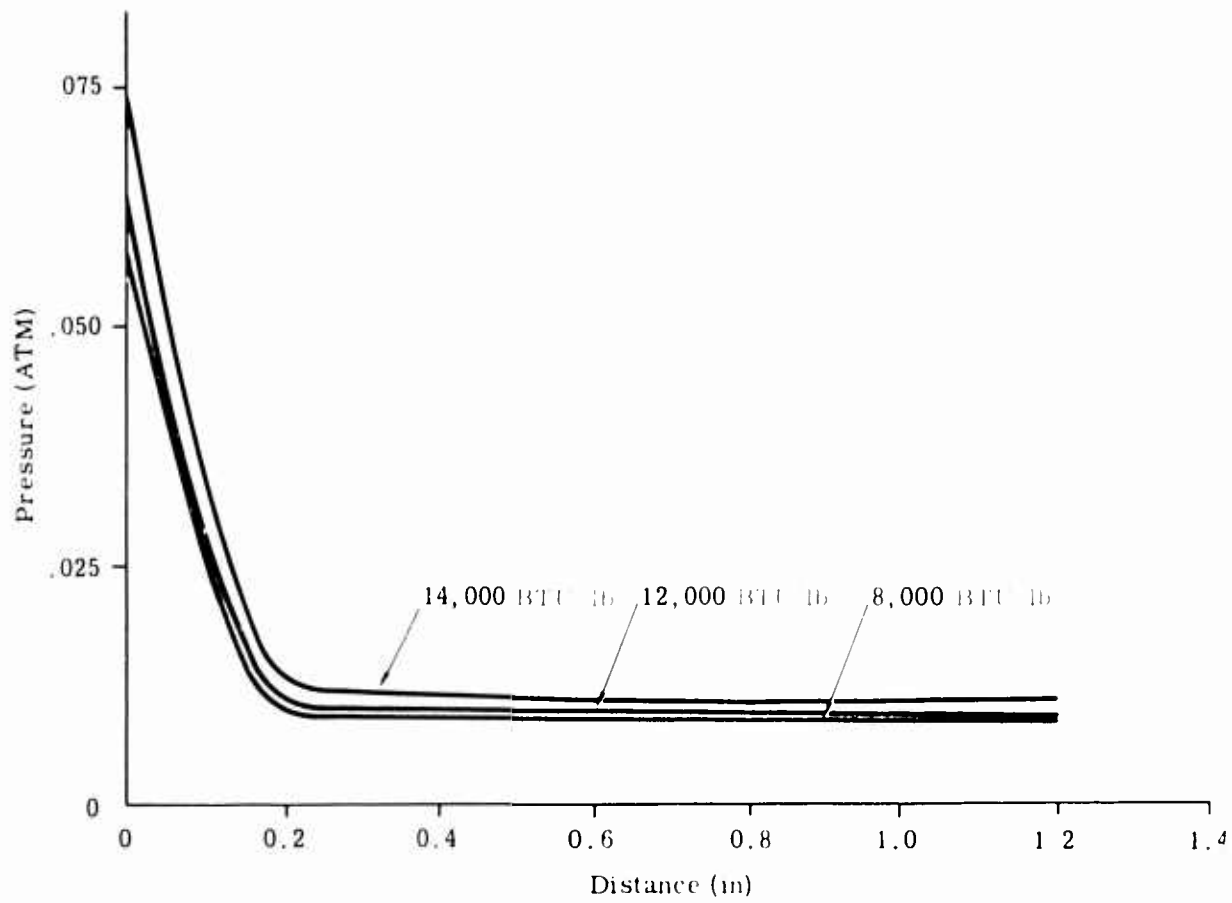


Figure 6. Surface Pressure on S-6 Model in 160 kw Jet
(Air - Nose Cone Section Enlarged)

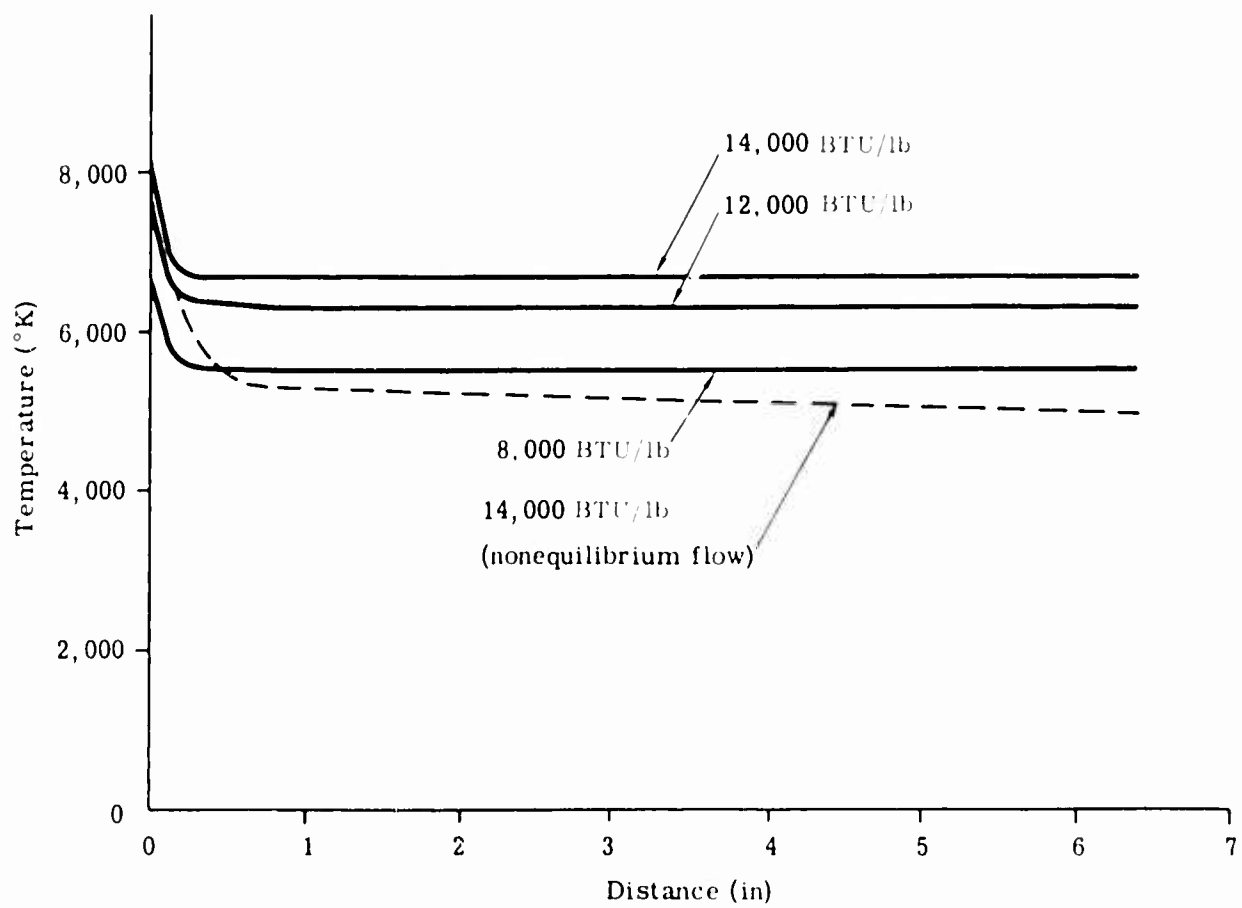


Figure 7. Kinetic Temperature Near Body Surface of S-6 Model in 160 kw Jet (Air)

TABLE I
Electron Density in Argon Gas

<u>Distance (Axial)</u>	<u>n_e</u>	<u>n</u>	<u>n_e/n</u>
3000 BTU/lb			
0	0.2×10^{15}	10^{17}	6.2×10^{-2}
0.125	5.2×10^{14}	3.75×10^{16}	1.39×10^{-2}
0.207	3.7×10^{13}	1.78×10^{16}	2.08×10^{-3}
0.750	3.75×10^{12}	1.77×10^{16}	2.12×10^{-4}
5500 BTU/lb			
0	8.35×10^{15}	6.8×10^{16}	1.23×10^{-1}
0.125	5.5×10^{15}	2.02×10^{16}	2.7×10^{-1}
0.210	6.3×10^{14}	1.06×10^{16}	5.95×10^{-2}
0.750	5.5×10^{14}	9.00×10^{15}	6.1×10^{-2}
8000 BTU/lb			
0	1.15×10^{15}	3.9×10^{16}	2.95×10^{-1}
0.125	3.05×10^{15}	1.4×10^{16}	2.16×10^{-1}
0.207	3.0×10^{15}	5.8×10^{15}	5.19×10^{-1}
0.750	10^{15}	5.2×10^{15}	1.92×10^{-1}

TABLE II
Electron Density in Air

Distance (Axial)	n_e	n	n_e/n
8,000 BTU/lb			
0	6.15×10^{13}	6.4×10^{16}	9.6×10^{-4}
0.125	9.25×10^{12}	2.5×10^{16}	3.7×10^{-4}
0.207	3.48×10^{12}	1.25×10^{16}	2.8×10^{-4}
0.750	3.08×10^{12}	1.14×10^{16}	2.7×10^{-4}
12,000 BTU/lb			
0	2.58×10^{14}	6.0×10^{16}	4.3×10^{-3}
0.125	5.03×10^{13}	2.35×10^{16}	2.1×10^{-3}
0.207	1.43×10^{13}	1.20×10^{16}	1.2×10^{-3}
0.750	1.16×10^{13}	1.08×10^{16}	1.07×10^{-3}
14,000 BTU/lb			
0	6.05×10^{14}	6.8×10^{16}	8.9×10^{-3}
0.125	1.07×10^{14}	2.7×10^{16}	4.0×10^{-3}
0.207	3.05×10^{13}	1.35×10^{16}	2.3×10^{-3}
0.750	2.66×10^{13}	1.24×10^{16}	2.2×10^{-3}

blunted cone (12-degree included angle) model. Kinetic temperatures are seen to fall by 40 percent for low-energy inputs and 25 percent for high-energy inputs in the equilibrium-flow calculations. These values are high by about 15-20 percent when they are compared to more realistic nonequilibrium calculations. Some of the latter were extrapolated directly from TRW/STL Laboratories, using calculations applied to prototype flight conditions (see Figure 3). Corresponding drops in ionization levels are given in Tables I and II.

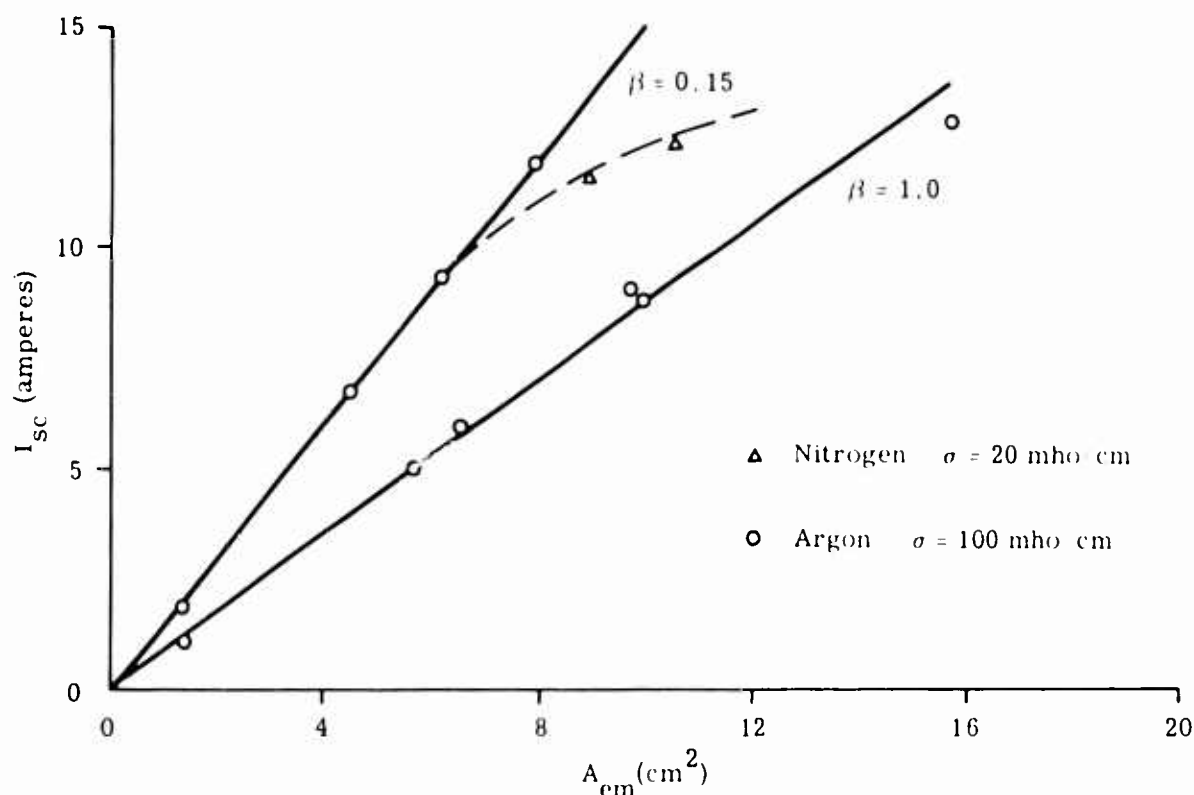


Figure 8. Short-Circuit Current Versus Emitter Area for Two Values of Effective β . Runs made in Argon Gas with 5000 BTU/lb Energy, and Nitrogen at 12,600 BTU/lb.

B. Parameters Influencing Generator Output

The detailed theoretical analyses made in References 1, 4, and 5 and in the Appendix of this report show a set of parameters that govern the output of the plasma generator independently and/or collectively. These may be listed as follows:

1. Emitter Area -- (A_{em}) is directly proportional to the thermionic emission rate in the Richardson-Dushman formula

$$I_{th} = (\text{constant}) A_{em} T^2 \exp \left(-\frac{\phi}{kT_{em}} \right)$$

and hence determines the magnitude of short circuit current output according to Equation 6.

2. Emitter to Collector Area Ratio -- ($\beta \approx A_{em}/A_c$) is proportional to the ratio of random electron current at the emitter to that at the collector. In Equation 2 this parameter acts like a resistance.

3. Emitter and Collector Surface Temperatures -- (T_{em}, T_c) electron emission is directly proportional to surface temperature according to the Richardson-Dushman equation above. From Equation 6, one can note that $T_{em} \gg T_c$ for minimum back emission.

4(a). Kinetic Temperature in Plasma -- (T_e) is the very source of the generator energy. Equations 2 and 3 show the open circuit voltage to be directly proportional to the electron temperature T_e and to depend logarithmically on the degree of ionization in the plasma which is also a direct function of T_e .

4(b). Degree of Ionization -- (n_e/n_o) determines the power output directly through the term $\frac{1}{2}$ (Equation 2) and indirectly by neutralizing the space charge created by the emission electron cloud at the cathode. It is proportional to the gas pressure and temperature.

4(c). Plasma Resistance -- (r_p) limits the effective length of the collector and consequently has a direct bearing on reducing the increased short circuit current output brought about by an increase in vehicle size, e.g., A_{em} .

5. Contact or Internal Resistance -- Either resistance is a significant constituent to the total generator internal impedance for the plasma jet scale models. It occurs primarily at the collector-to-sting contact point (see Figure 2a).

6. Emitter and Collector Material -- These govern the output through two factors -- the work function, which in turn governs the electron emission rate and under proper conditions can supply as much as 1.5 volts through $\phi_c - \phi_e$ in Equation 1, and the electrical properties which contribute to the total internal impedance of the generator. Because the ASP is a low-voltage, high-current device, the internal impedance should be kept minimal.

It is obvious that there is a strong interdependence among the various parameters listed above. For example, a favorable effect expected by a change in one parameter might cause an adverse effect on another. The following experimental results show these various effects, and with the theoretical predictions, can lead one to establish optimum working conditions for the hypersonic plasma generator.

C. Experimental Results

The results reported here were collected during a year in Sandia Corporation's 160 kw plasma jet facility. Final experiments are now under way in the 1-mw facility with larger models to study in greater detail the effects of parameters 1 and 2.

1. Emitter Area -- Table III lists the various sizes of emitters and collectors used. The emitter areas vary between 0.8 and 2.50 in² and β varies between 1 and 0.03. As predicted from Equation 5, the short circuit current shows a linear dependence of I_{sc} on the emitter area (Figure 8). According to Equation 4, this linear dependence should change as the plasma resistance becomes significant ($r_p > 0.01$ ohm). This effect was noticed clearly in nitrogen, but was insignificant in argon because of the high degree of ionization in the latter. Because of the limited size of the jet and consequently of the models, only "trends" were obtained in nitrogen gas represented by the dotted lines in Figure 8. The open-circuit voltage showed no dependence on the emitter area as predicted from Equation 2. Figure 9 compares outputs from two geometrically similar models with different emitter areas.

TABLE III

Model Dimensions		
Model	Emitter Area (in ²)	Collector Area (in ²)
S-0	0.85	5.89
and	1.70	9.82
U-0	1.03	9.82
	1.18	9.82
Pyrographite		
U-10	Same	9.95
S-10	0.70	4.95
S-30	0.86	0.84
	2.48	2.44
S-6	1.30	16.60

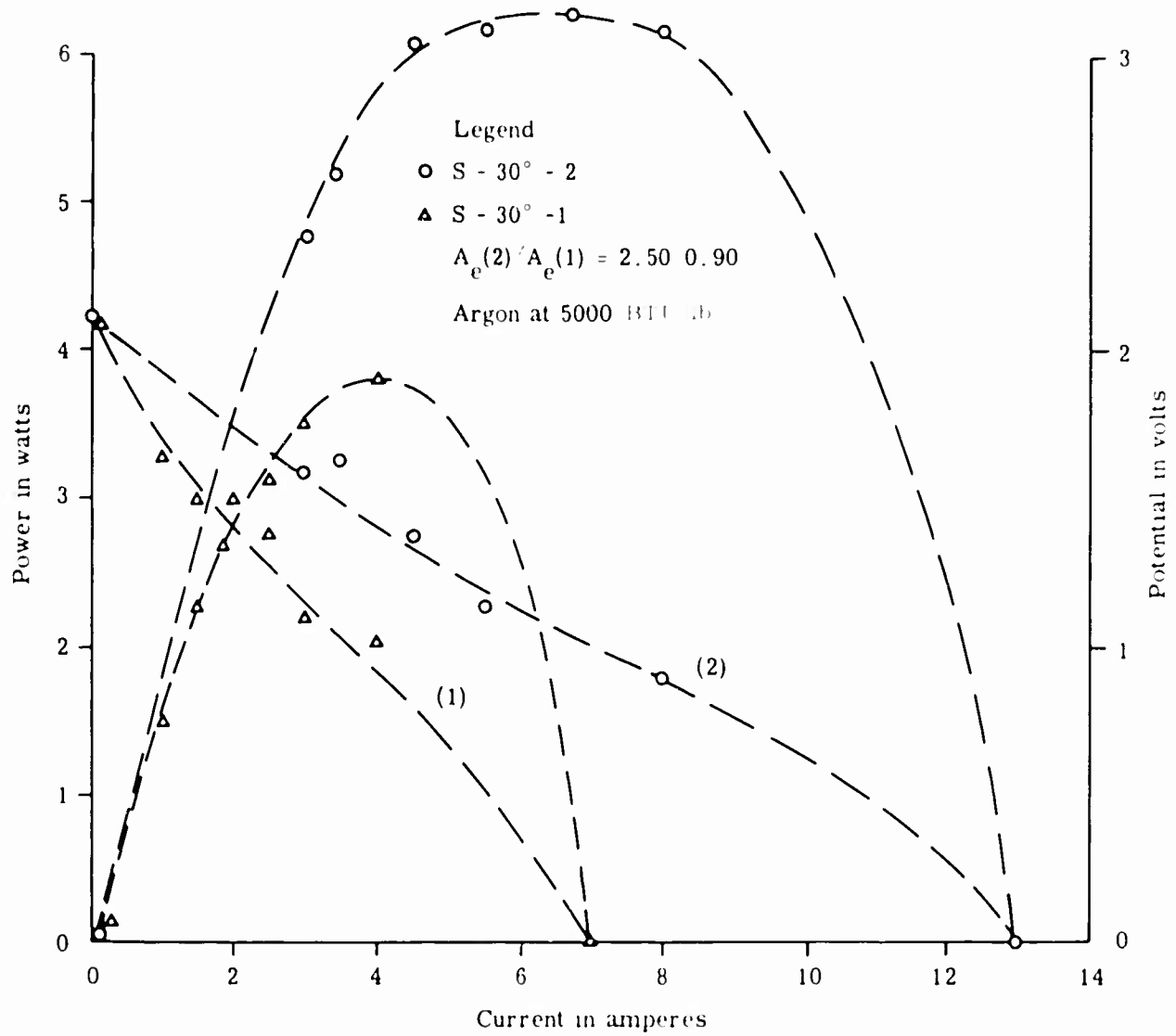


Figure 9. Output from Geometrically Similar Models with Different Emitter Areas

2. Emitter to Collector Area Ratio -- A large number of runs were made to determine the effect of β on power output, especially on the short-circuit current. Figure 8 shows this effect graphically. In general, the trend follows theoretical predictions, however, for most models the effect of flow separation over the model afterbody, the contact resistance between sting and collector (see Figure 2a), and the plasma resistance becoming effective for $\beta \geq 0.2$, could not be identified separately and, consequently, an effective $\beta = \beta^*$ was used to correlate data. For negligible r_p and r_c , the data fit the curve $i = I_{th} = 1/(1 + \beta)$ best for "wetted" collector areas only. These were determined visually by observing detachment and reattachment points and collector surface glow. For increasing plasma resistance (e. g., air and nitrogen runs) the points on I_{sc} vs A_{em} curve fell below the respective β lines, indicating the effect of r_p . This point is discussed in greater detail below, under 4(c).

3. Emitter and Collector Surface Temperature -- These temperatures were measured with a two-color pyrometer attached to a recording chart. When the arc jet glow overshadowed surface color temperatures, the jet was turned off instantaneously and the surface temperature estimated from the time-temperature decay history, with an accuracy within $\pm 100^\circ\text{C}$. Depending on the arc jet energy and model material, average values of T_{em} varied between 2300 and 3200 $^\circ\text{C}$. Stagnation point temperatures exceeded 3400 $^\circ\text{C}$ on sharp cone models (Figure 2c). This temperature was deduced from observing melting tungsten. T_c was less than 1200 $^\circ\text{C}$ for S-0 models (see Figure 2), about 1500 $^\circ\text{C}$ for model S-6 surfaces, and 1800 $^\circ\text{C}$ for S-30 models. Back emission from the collector becomes significant for $T_c/T_{em} \geq 0.8$. Maximum tested cone angles were 30 $^\circ$ with $T_c/T_{em} \leq 0.7$. Figure 10 shows the output for four geometries having comparable $A_c/(1 + \beta)$. Hammerhead geometries are shown to reduce output because of reduced effective β arising from flow separation. $A_p/(1 + \beta)$ for S-30 was twice that of S-10 with a slightly lower output, probably because of considerable back emission from the S-30 and very large β ($\beta = 1.0$).

4(a). Kinetic Temperature in Plasma -- Accurate estimates of this parameter were difficult to make. Calorimetric and pitot pressure studies (Reference 6) combined with spectrographic estimates (Reference 7) gave values of 12,000 $^\circ\text{K}$ electron temperatures at the stagnation point of the ASP vehicle in 5000 BTU/lb argon gas. In air, stagnation temperatures were estimated at 7500 $^\circ\text{K}$ for 12,000 BTU/lb energy input. Unfortunately, no spectrographic results are available at present to check this magnitude which may be somewhat optimistic. Figure 7 gives plots of T_p over an S-6 shape model for air, using both equilibrium and nonequilibrium reaction calculations. The maximum temperature drop from stagnation point to afterbody is of the order $T/T_0 \approx 0.5$.

To estimate open-circuit voltage values under optimum run conditions, which in argon would correspond to $V_T = 1$ ev, $\gamma = 1/293$, and in air $V_T = 0.7$ ev, $\gamma = 1/155$, the following table is obtained:

TABLE IV
Open-Circuit Voltage

	Argon		Air	
	δ	V_{oc} (volts)	δ	V_{oc} (volts)
$V_{em} = 0$	0.10	3.42	0.10	1.92
(Eq. 2)	0.01	1.37	0.01	0.67
$V_{em} = 0$	0.10	6.51	0.10	4.22
(Eq. 3)	0.01	5.95	0.01	2.03

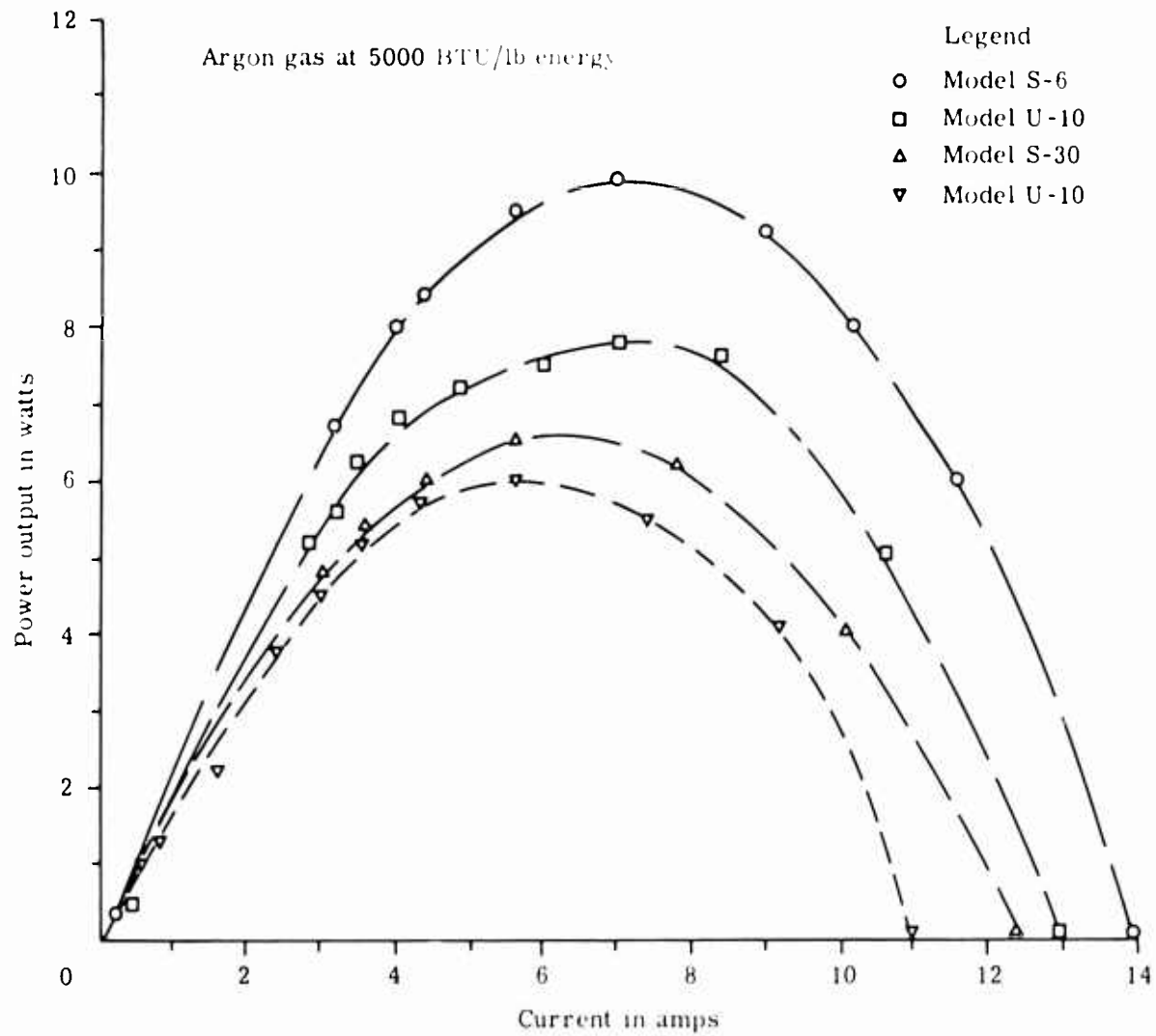


Figure 10. Power Output for Various Model Geometries at Constant Jet Energy.

Measured values in argon averaged about 3.3 volts with the exception of a value of 4.4 volts registered with model tip flush with nozzle exit where V_{ip} might have been closer to 1.3 ev (1 ev stagnation point temperatures were measured at a point 1 inch downstream of nozzle exit where most of the tests were run). This indicates that the emitter sheath V_{em} was possibly negative. A note of caution, however. Equations 2 and 3 are based on the assumption T_e is the same at both emitter and collector. For $T_{ec} = 0.7 T_{em}$ it is possible to obtain 4 volts open-circuit voltage with $V_{em} = 0$ and $\delta = 0.1$ (see Appendix). Corresponding measurements in air gave optimum values of 1.9 to 2.3 volts open circuit.

4(b). Degree of Ionization -- From above values of T_{el} (Tables I and II), the percent ionization in the gas around the ASP model can be summed up. In section 4(a) above values of γ were based on complete charge neutralized flow conditions. This, however, was not the case for all test conditions, as was evident from special seeded gas runs where values of V_{oc} increased by 15 to 25 percent, depending on energy input, and I_{sc} by as much as 100 percent (see Table V below).

TABLE V
Output with and without Seeding

Gas	Energy BTU/lb	No Seed		1% K_2CO_3 Added	
		V_{oc}	I_{sc}	V_{oc}	I_{sc}
Argon	5,000	1.9	14.0	2.2	18.0
	4,500	2.5	10.0	----	15.0
Nitrogen	14,000	1.15	4.0	1.55	7.5
	12,000	1.20	3.0	1.70	6.4

Two types of seed material were used, KCl and K_2CO_3 . Because of the electronegative properties of KCl where V_{oc} -seeded gave 10 percent lower values than V_{oc} -no seed, the KCl was discarded. K_2CO_3 powder was fed downstream of the arc at the rate of 1 gm/min, or a maximum of 1 percent by weight of the gas mass flow. The effect of ionization on short-circuit current output is further illustrated in Figures 11 and 12 where, in addition to seeding, special runs are shown which were made with various mass ratios of A- N_2 gas. Figure 13, on the other hand, compares runs in argon, air and nitrogen on the same model and comparable energy inputs, with maximum output decreasing from 13 watts to 3 watts, respectively.

4(c). Plasma Resistance r_p -- Referring to Equation 4, the short-circuit current is seen to depend on the plasma resistance through the term r . If one assumes r to be represented by

$$r = L/\sigma$$

$$= \frac{aR}{\sigma}$$

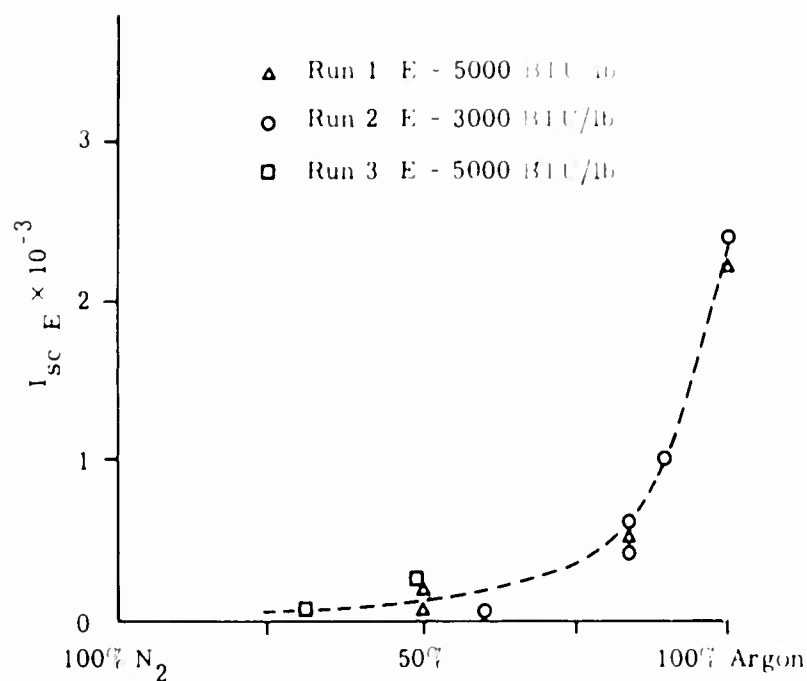


Figure 11. Degree of Ionization on Short Arc at Current Output, Argon-Nitrogen Mixtures

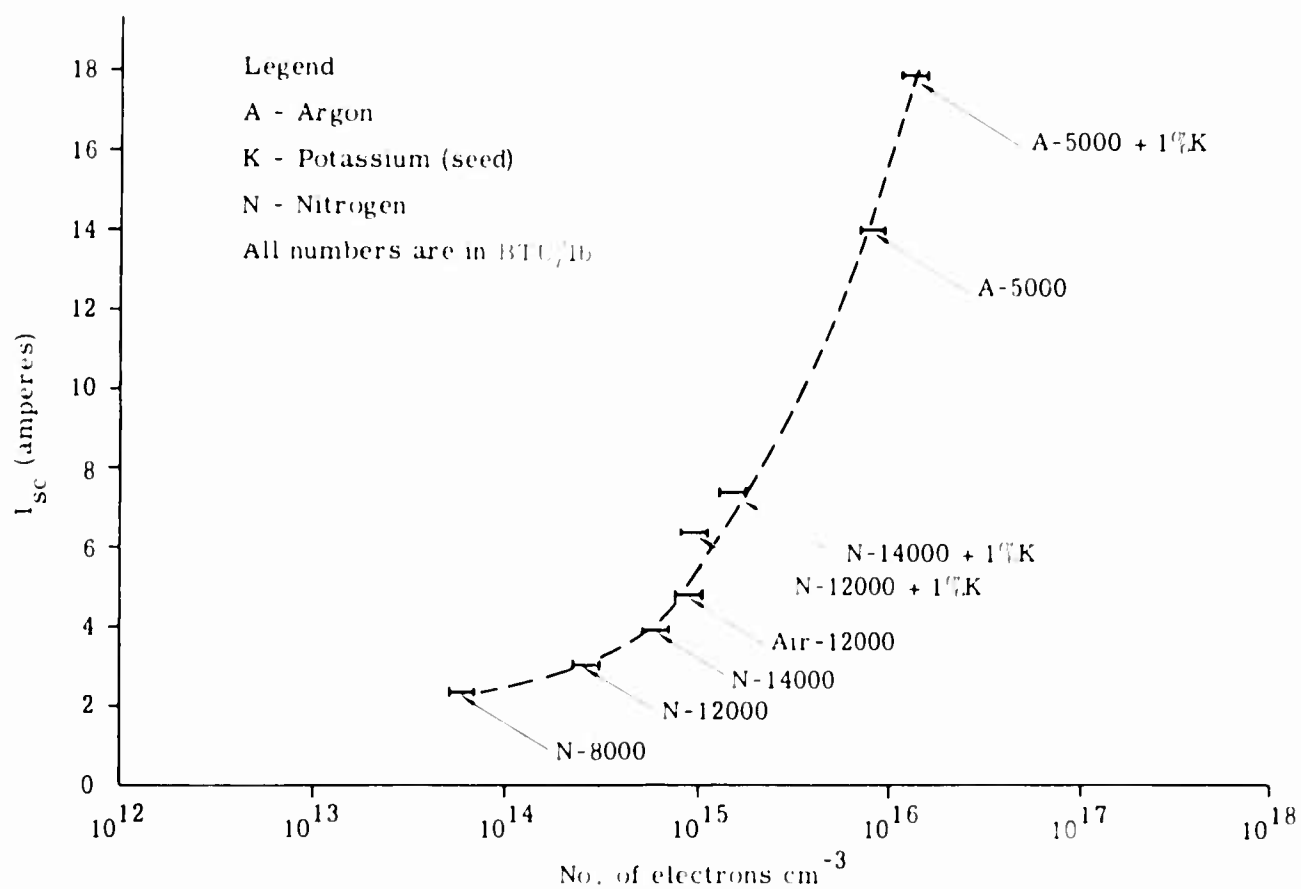


Figure 12. Short Circuit Current versus Electron Density (Unseeded Gas from Spectroscopy, Seeded Gas Using Saha Equation)

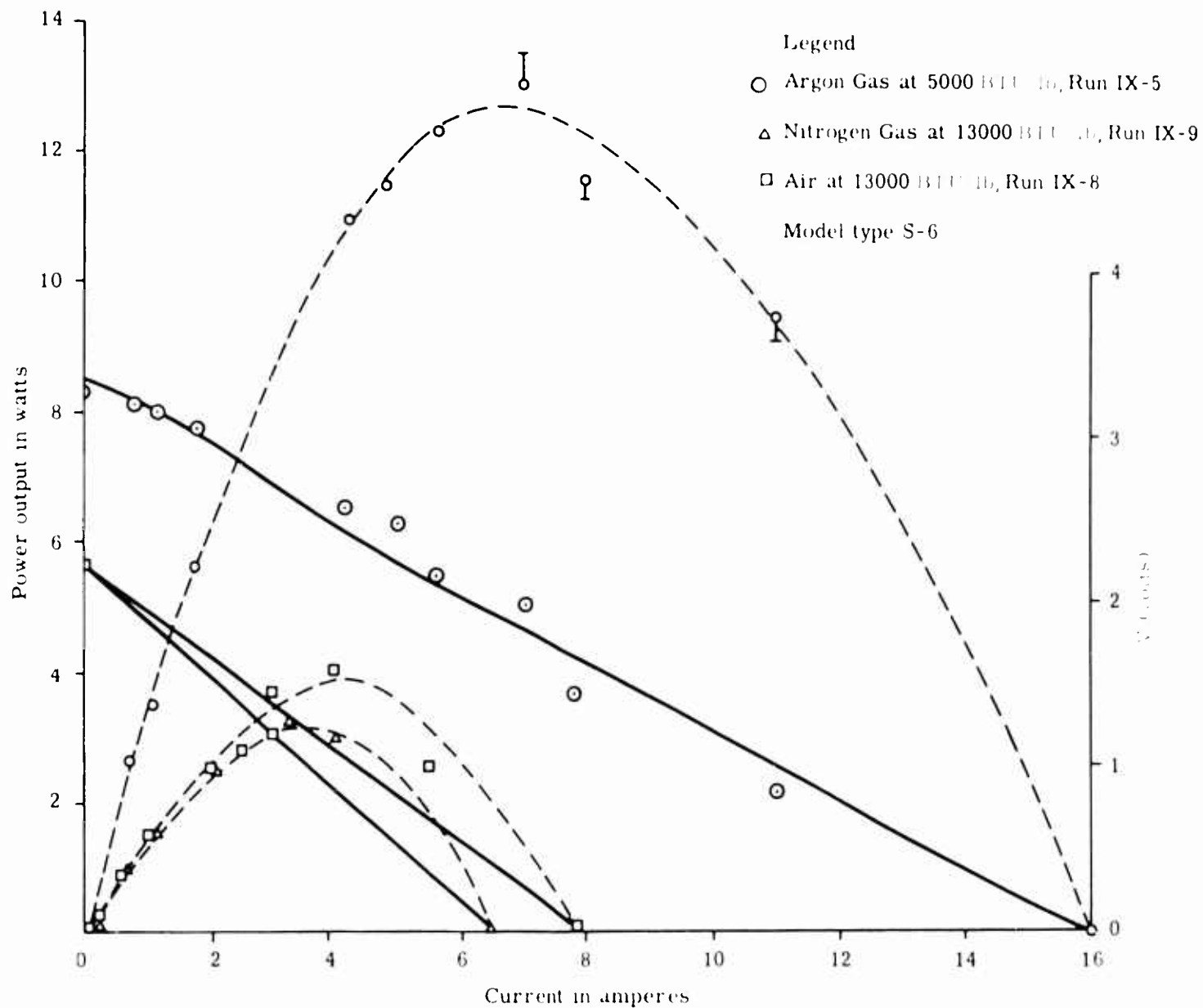


Figure 18. Power Output and V-I Characteristics of S-6 Model in Argon, Nitrogen and Air

where

$R = \text{emitter radius (cm)}$

$\sigma = \text{plasma conductivity (mhos/cm)}$

$\alpha = \text{some fraction less than one, depending on trajectory}$

Equation 4 can be rewritten

$$C_{\text{sc}} = I_0 \ln \left[\frac{1 + \gamma \delta + \frac{1}{\beta I_{\text{sc}}}}{\gamma \delta + \frac{1}{\beta I_{\text{sc}}}} \right] \quad (7)$$

where $C = \alpha R I_{\text{th}} \sigma V_{\text{p}}$. Equations 5 and 7 are plotted in Figure 14. It is clearly seen that, for a given β , the short circuit current falls below the $r_{\text{p}} = 0$ (or $\sigma = \infty$) value if plasma resistance is included. The constant resistance curves show a significant reduction in short circuit current for a given β . In fact, a small β in a low plasma conductivity or larger electron trajectory (αR) is useless as seen from curve $C = 10$. For $\gamma = 1.155$ the curves in Figure 14 lie about 5 percent below the $\gamma = 1.293$ curves. From sections 4(a) and 4(b), σ in argon was estimated as 100 mho/cm and in air as 20 mho/cm. For a 10 cm effective electron trajectory this corresponds to $r_{\text{p}} = 0.1 \text{ ohm}$ and 0.4 ohm , respectively. If one compares the i_{sc} output in argon and in air for a given β and R , $i_{\text{sc}}(\text{argon}) \approx 2 i_{\text{sc}}(\text{air})$. This difference is believed to result partially from reduced thermionic emission in air as compared to argon because of possible lack of charge neutralization in the former (ionization in argon is a factor of 10 greater than in air), and partially because of r_{p} . For example, for $R = 1 \text{ cm}$, $\alpha = 0.2$, $I_{\text{th}}(\text{argon}) = 2 I_{\text{th}}(\text{air})$, $\sigma_{\text{Ar}} = 100$, $\sigma_{\text{air}} = 20$, $V_{\text{p}} = 10$, $V_{\text{t}} = 0.7$ then $C_{\text{argon}}/C_{\text{air}} = 0.23$. A new set of experiments, presently under way in the Sandia Plasma Laboratory 1 mw facility with model sizes 2 to 10 times longer than those used in the 160 kw facility, will enable us to determine this effect with greater accuracy (see below). Several runs with insulator lengths varying between 0.2 to 2.0 inches in argon indicated no significant changes in i_{sc} output. In nitrogen, on the other hand, there was observed a 15 percent reduction in i_{sc} when insulator length was increased from 0.25 inch to 1.5 inches for a fixed contact resistance r_{c} .

5. Contact Resistance - A large resistance, r_{c} , was introduced from the contact points between emitter and the pick-up rod and between the collector and the strap which supported the model and served as the connector for carrying current to external load. These values were minimized by using cadmium solder, which melted upon heating and made a liquid contact, or, 4P-Hg-In liquid metal alloy at the two contact points. Minimum values of r_{c} were of order 0.1 ohm and often as high as 0.5 ohm. Maximum power output generally occurred at $r_{\text{c}} = 0.2 \text{ ohm}$, indicating a possible $r_{\text{p}} + r_{\text{c}} = 0.2 \text{ ohm}$ under conditions of optimum internal impedance control. Much more reliable values are forthcoming in the large scale model tests now underway in the 1 mw facility.

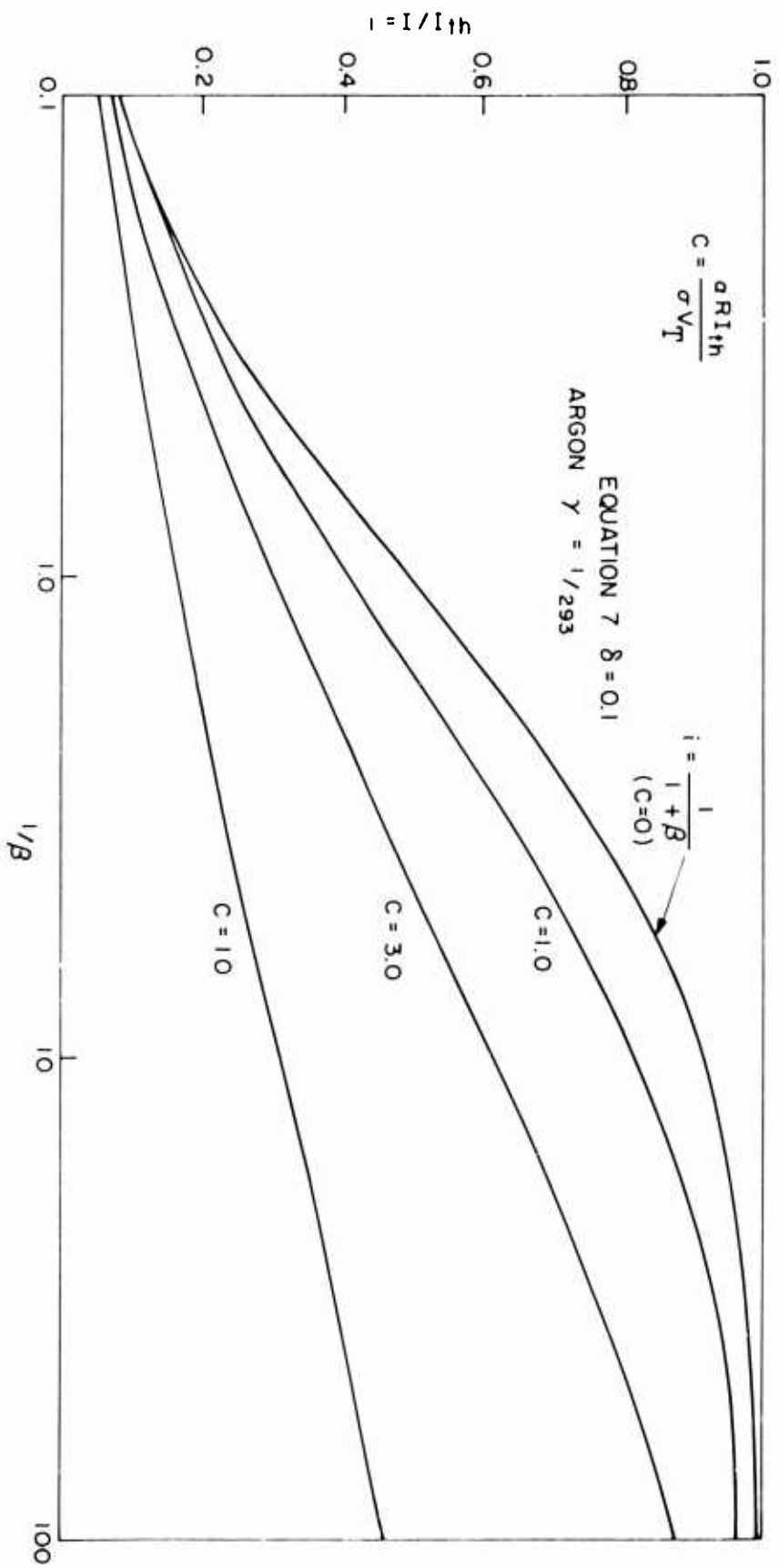


Figure 14. Dimensionless Short-Circuit Current Versus l/b for Various Resistance Parameters C , in Argon, and σ , V_T

6. Materials -- Table VI lists the type of materials used as emitters, insulators, and collectors.

TABLE VI

Model Materials

Emitter	Collector	Insulator
ATJ graphite	ATJ graphite	Boron nitride
Pyrolitic graphite	Pyrolitic graphite	Al ₂ O ₃ - 99.6%
Phenolic carbon	Phenolic carbon	99.8%
Tungsten	Tungsten	BMI 785*
Tantalum	Tantalum	Al ₂ O ₃ + 5 volume
Zirconium-carbide + graphite, eutectic	Niobium	percent Mo
	Molybdenum	
	Cb - 10, W - 2, 5, Zr	Al ₂ O ₃ + 3 volume
	Ta - 10 W	percent W
	Mo - 0.5, Ti - 0.03, Zr	

* A special porous insulator developed by Battelle Memorial Institute, Columbus, Ohio.

The fundamental characteristics required in emitter and collector materials are: general thermal resistance and mechanical integrity, good electrical conductivity and low thermionic work functions. Of these three, experiments showed the last two to be the least important because little could be done to preserve surface integrity in the highly reactive atmosphere of a dissociated-ionized air. Most refractory metals formed high resistance oxide layers on the collector and lost power output after 15 seconds of run time. This was not the case with S-30 models with 1800-2000°C surface temperatures where oxides became volatile. Phenolic impregnated with graphite had higher electric resistance than pure graphite and gave 70 percent of the output obtained from graphite models (see "Optimum Results" below). The best output was obtained in a graphite (emitter) - TZM (collector) model primarily because of good collector-to-sting contact and volatile oxides. Pyrolitic graphite emitters produced a uniform emission but the α -direction conductivity offered resistance as high as phenolic carbon.

The insulators were chosen primarily for good thermal shock properties. Of these BMI-785 ranked best, followed by boron nitride and Al₂O₃ + 5 percent molybdenum dispersion. The porous nature of the first made it difficult to keep close mechanical tolerances and hence the last two were used most extensively.

D. Optimum Results

Data reduction showed blunted cone emitters (0.25-inch emitter radius) followed by 6^{10} - 10^{10} conical aerobody, $\beta < 0.15$, and graphite or tungsten surfaces to yield the highest output (Figures 15 and 16). Figures 15-18 represent samples of outputs graphically. The solid lines are curve fits using Equation 1 with $\beta = 0.1$, γ (argon) = $1/293$, γ (air) = $1/155$ and $\delta = 0.05$ to 1.0 .

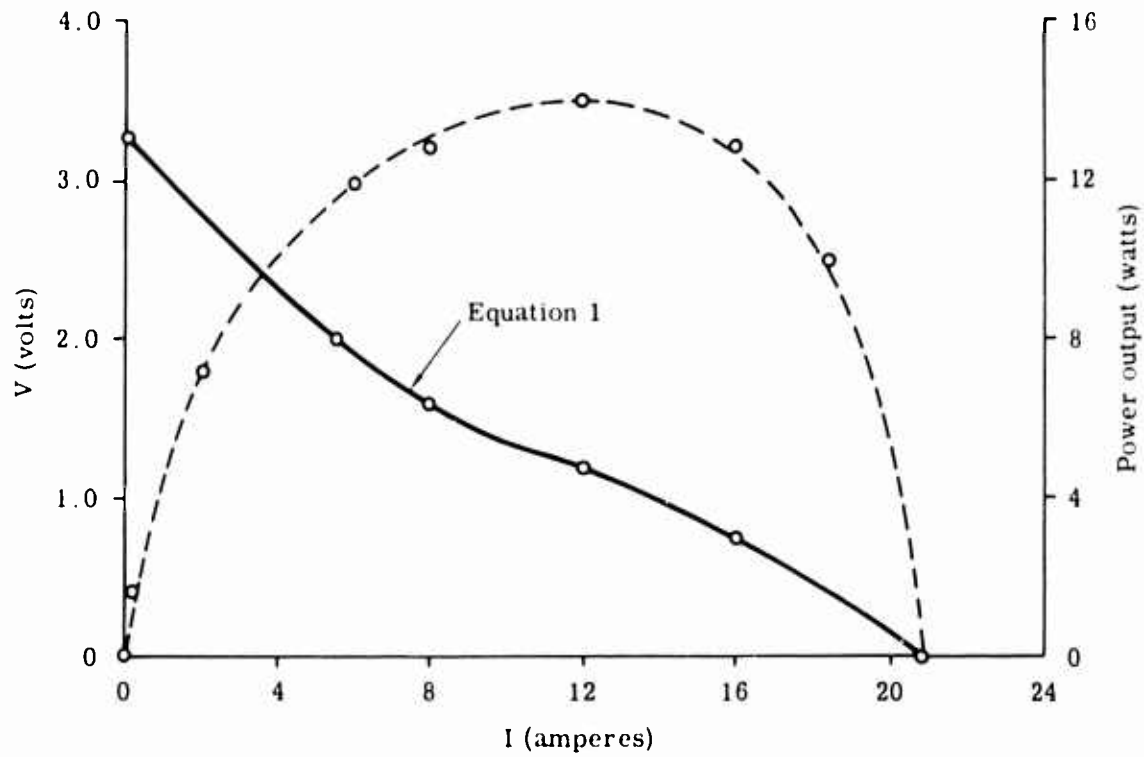


Figure 15. Output Data for $\beta = 0.15$, $V_T = 1$ ev, $b = 0.1$ from S-6 Tungsten Model in Argon at 5000 BTU/lb

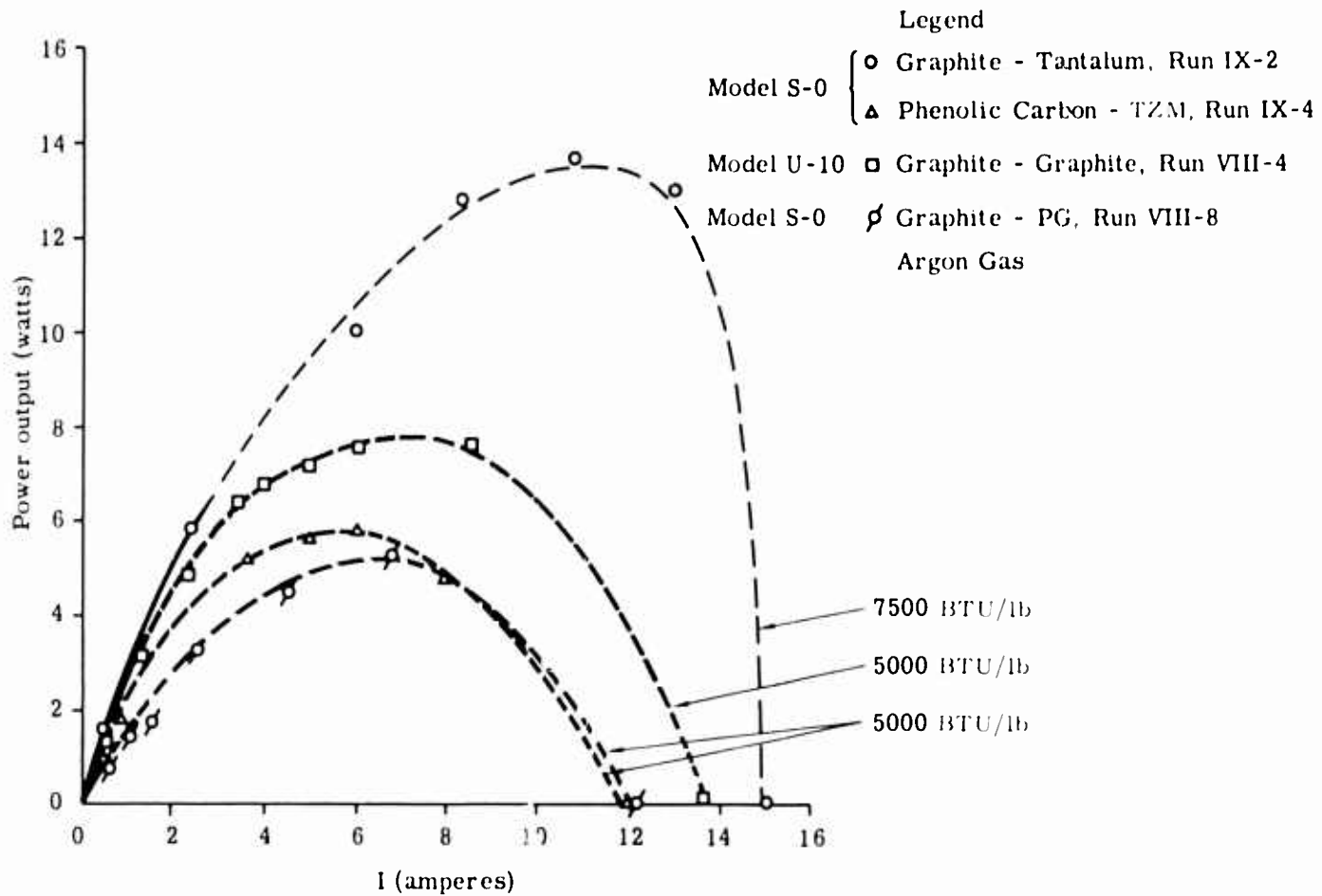


Figure 16. Power Levels from Various Models Showing the Effect of Argon Gas Energy on Output

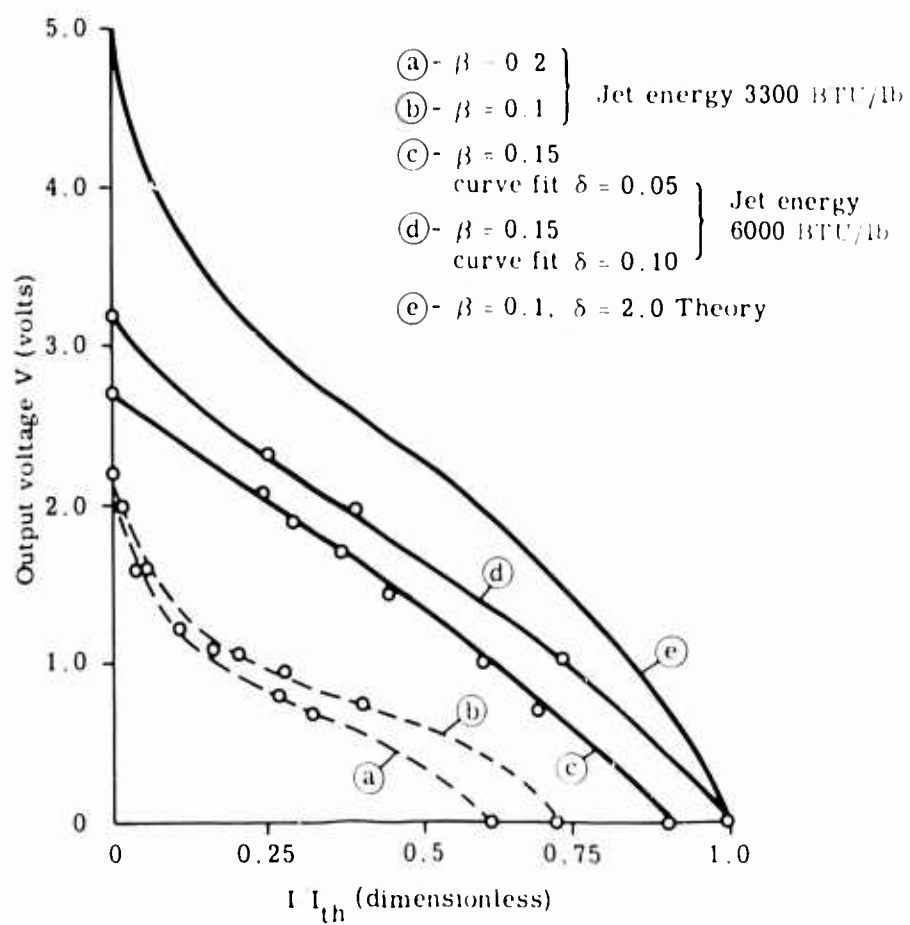


Figure 17. Voltage-Current Characteristics for $V_T = 1.0$, Various β and δ Values in Argon Gas

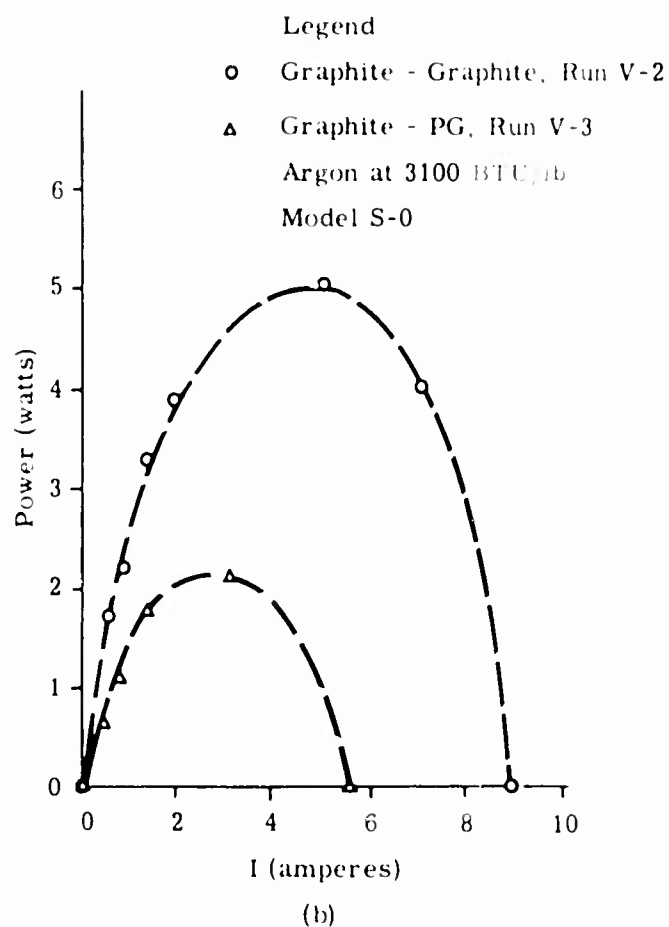
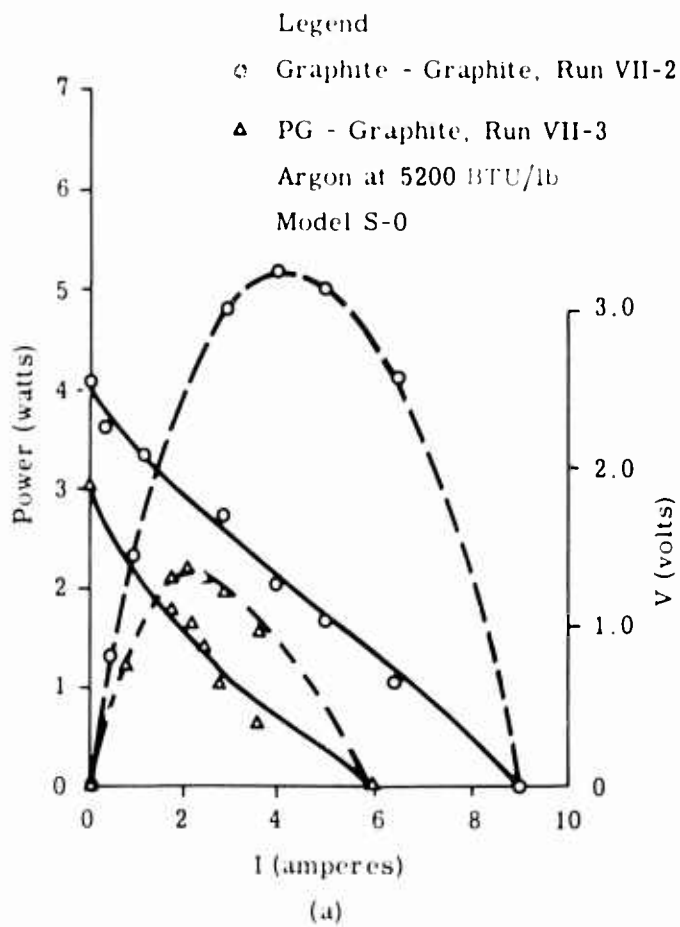


Figure 13. Effect of Contact Resistance between Pyrolytic Graphite Shell and Carbon Substrate on Output

To estimate the maximum power output of this generator the expression $P = I_{th} (E - I_{th} R)$

$$E = V + iR$$

$$i = I - I_{th}$$

is maximized (see Reference 1) and plotted as a function δ (thermionic to random electron ratio) for various values of β and r (or r_p) in Figure 19. For plasma densities encountered in a plasma jet $\delta \approx 0.1$. The effect of r_p on β is seen to increase as β decreases (or as the collector size increases). (See also Figure 14.) Once again there is not enough reliable data for r_p to allow a direct experimental check of Figure 19. The trends, however, are in the expected direction as observed in Figures 13-19, and especially in Figure 18 where β is an "effective" value, taking into account r_p and r_c .

Maximum short-circuit current measured was 24 amps over a hemispheric emitter $R = 3/8"$ at $3250^\circ K$. According to the Richardson-Dushman equation

$$I_{th} = C^* A_{em} T_{em}^2 \exp(-e\phi_c/kT_{em})$$

this should yield $I_{th} = 78$ for $C^* = 120$. However, if one assumes T_{em} to be a function of θ , the azimuthal angle, and assumes a parabolic temperature drop from stagnation point $\theta = 0$ to $\theta = \pi/2$ or $T_{em} = 3250 - 200 \theta^2$, the above equation yields

$$I_{th} = 240 \pi R^2 \int_0^{\pi/2} T_{em}^2(\theta) \exp\left[-\frac{e\phi_c}{kT_{em}(\theta)}\right] \sin \theta d\theta$$

or $I_{th} = 27$ amps. Table VII summarizes the optimum output per emitter area with several different materials both in argon and in air.

TABLE VII
Optimum Output per Emitter Area

Model	Material	Argon (5,000 BTU/lb)			Air (12,000 BTU/lb)		
		I_{sc} amp./in. ²	V_{oc} volts	Maximum Power watts/in. ²	I_{sc} amp./in. ²	V_{oc} volts	Maximum Power watts/in. ²
S-6 (12° blunted cone) $\beta = 0.15$	Graphite (emitter, collector)	21	3.25	15	4.0	1.3	2.3
	Phenolic carbon emitter, graphite collector	15	3.25	8	3.0	1.0	1.5
S-30 ⁰ HRV shape $\beta = 1.2$	Tungsten (emitter, collector)	21	3.0	7	4.5	1.7	2.3
	Phenolic carbon (emitter, collector)	--	---	--	3.8	1.4	1.4

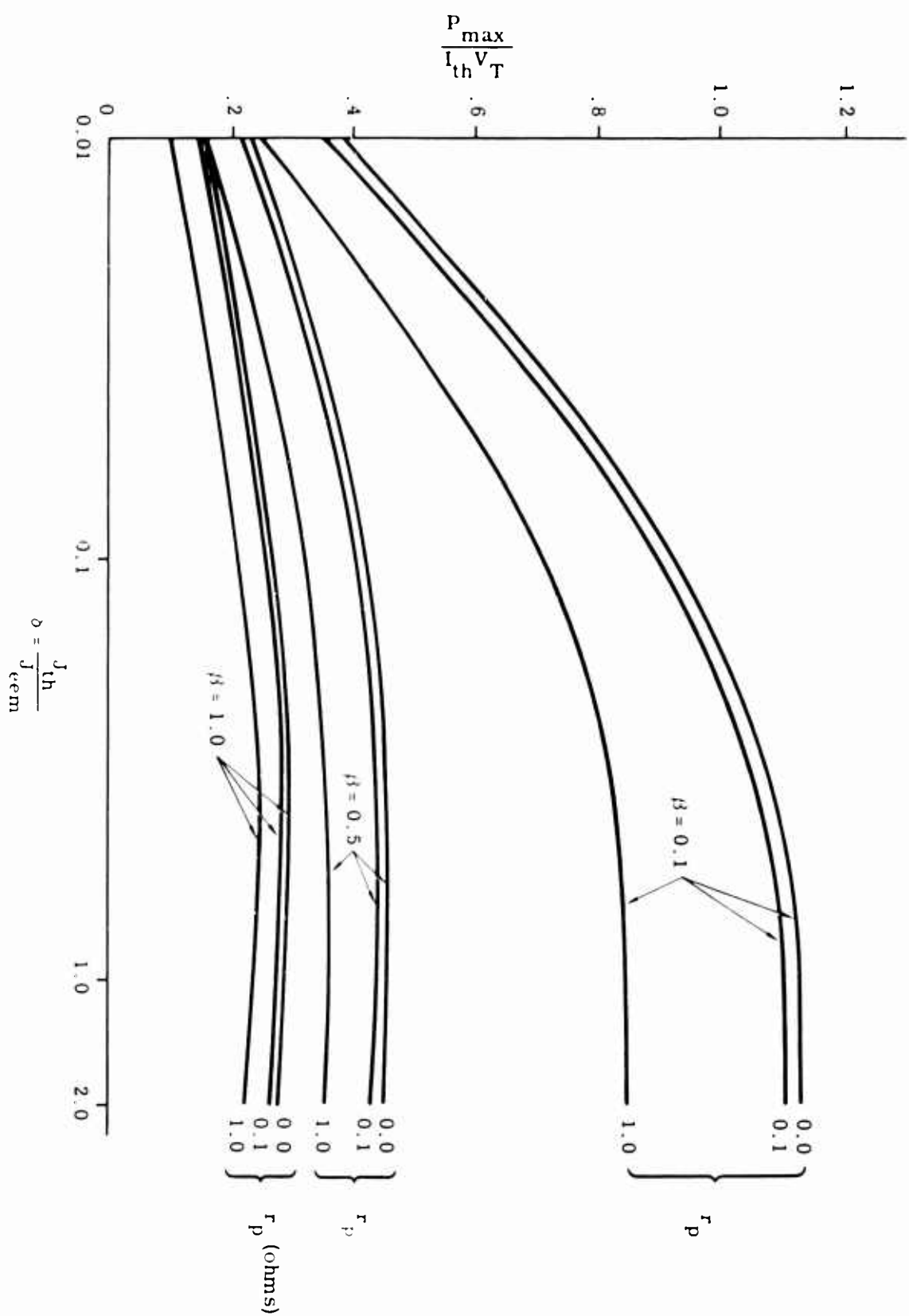


Figure 19. Dimensionless Maximum Power versus b for various values of β and r_p

Two things are obvious from Table VII. First, phenolic carbon is seen to average about 70 percent of the short-circuit current of graphite and 60 percent of the power output with no significant change in open-circuit voltage. The former two show the effect of $m = 0.4$ impedance offered by the material and the latter points to the fact that V_{oc} depends primarily on the plasma energy. Second, comparing the S-6 shape with $\beta = 0.4$ to the S-30⁰ sharp cone model with $\beta = 1$, it is easy to see how a large collector-to-emitter area ratio (small β') affects output in the case of argon. However, this ratio is more than compensated for in air because of considerably lower plasma conductivity of the latter.

The highest short-circuit current recorded to date in argon was 28 amps/in² of emitter area and the highest open-circuit voltage, 4.4 volts. In air, these values were 8 amp/in² and 2.3 volts, respectively. Repeatability of runs for identical models were governed chiefly by reliability of consecutive runs in the plasma jet and repeatability of contact resistance. Under best conditions of control, repeatability varied between 10 and 20 percent. When contact resistance was under close control, low arc jet reliability was caused primarily by electrode erosion.

Free Flight Conditions

It is difficult to assess the exact range of applicability of plasma jet experiments to free flight conditions where the air is shock ionized and has comparatively lower kinetic temperatures than those found in an arc jet. Figure 20 is a plot of electron temperatures and degree of ionization over a 3-inch diameter blunt hemisphere cylinder on a re-entry trajectory with 22,457 ft/sec re-entry velocity. Between altitudes of 250 to 100 kilofeet, phenolic carbon emitter can be made to yield a maximum of 150 amps short-circuit current with 2.0 volts open-circuit voltage (75 watts) by directly scaling-up the plasma jet data obtained in air. According to Figure 21, however, electron conductivities in the boundary layer are not expected to exceed 100 mho/cm. The plasma resistance over an effective electron path of 5 inches will then be at least 0.1 ohm, reducing the vehicle output to 20 watts. This will require increasing the voltage output to drive the large thermionic currents by either dividing the surface into several emitter-collector pairs or using supersatellite re-entry speeds generating 6-10 volts open-circuit voltage. Either of these methods will cause the output of a full-size re-entry vehicle (3.0-ft diameter) to be 1 kw or more. Because of high recombination rates, no output is expected below 50,000 feet altitude unless some form of seeding is used from the nose cone. Furthermore, high pressure near the stagnation point is expected to inhibit thermionic emission by a factor λ/R (λ is mean free path at emitter wall).

Future Work

Some of the results reported here are not yet final. A set of plasma tests in a larger (2-2.5-inch diameter) jet are expected to yield more reliable results on the combined effects of increasing collector and emitter areas and thereby lengthening average electron paths from emitter to collector but still holding contact resistance to a minimum. From trends obtained to date it is expected that increased values of r_p will slowly decrease the I_{th} versus A_e curves (Figure 8).

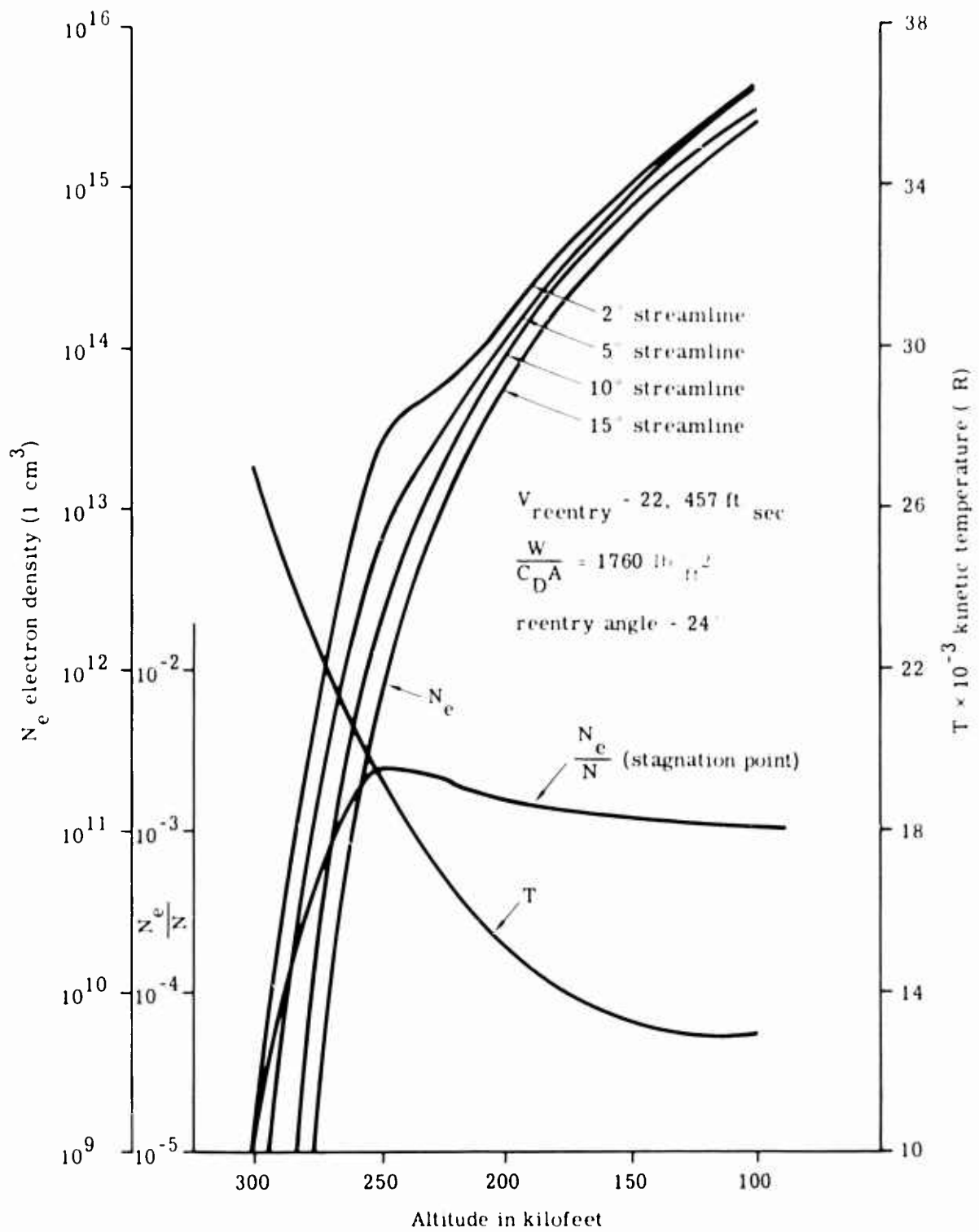


Figure 20. Electron Density and Kinetic Temperature Near Stagnation Point for Blunt Re-entry Vehicle at Various Altitudes

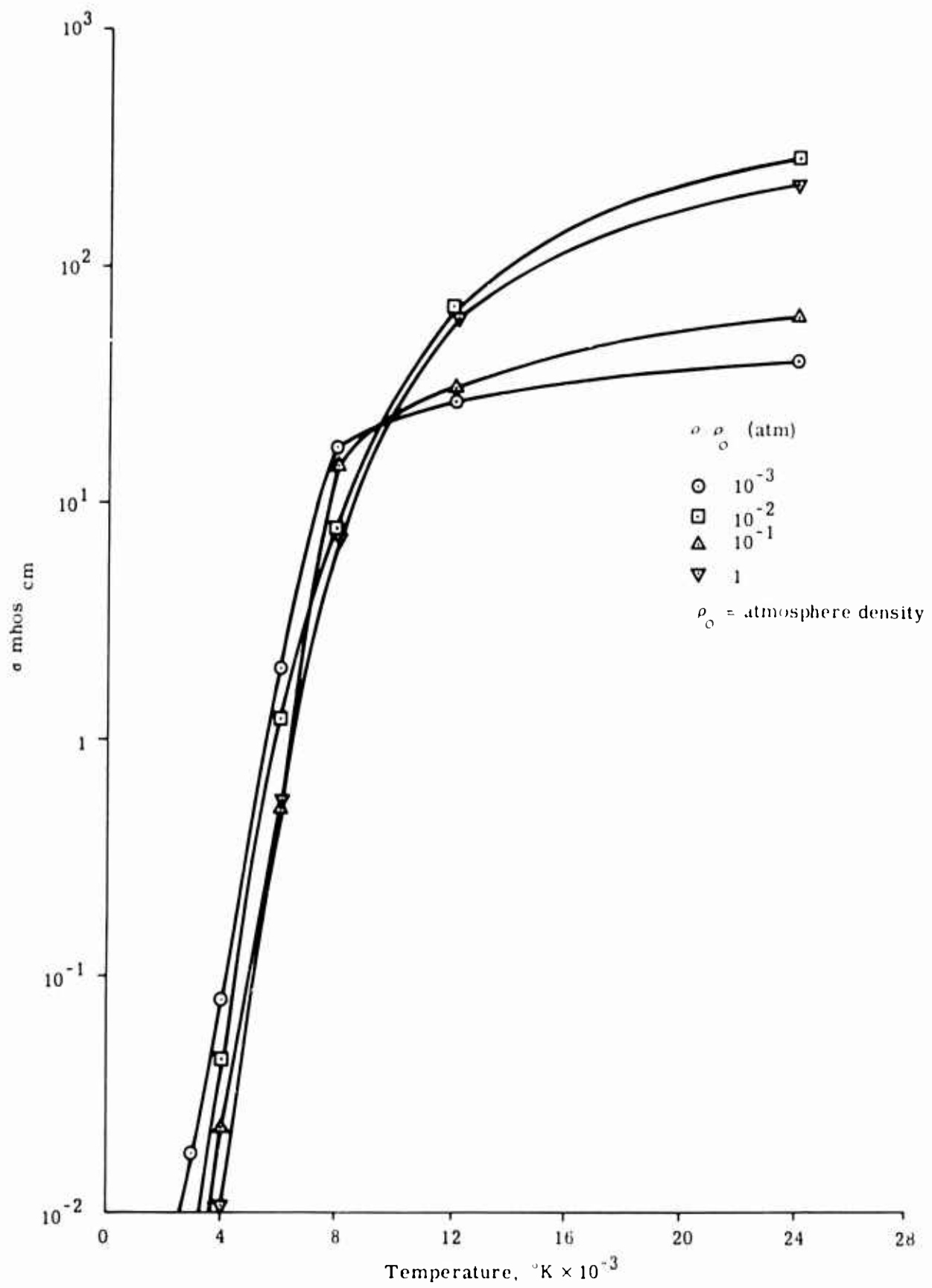


Figure 21. Electrical Conductivity as a Function of Temperature for Equilibrium Air at Various Densities. (Equation B-5)

Several runs will also be made with cesium impregnated tungsten emitters to simulate in-flight seeding conditions, and a new set of heat resistant carbide surfaces will be tested. Finally, models have been designed with two emitter-collector pairs to evaluate the "in-series" behavior of such a generator. These results will be given in a separate report before the end of the year.

APPENDIX

Three analytical points will be discussed briefly in this Appendix: the sheath potentials at the emitter and collector, the effect of joule heating and Thompson emit in the plasma generated by the large currents dumped into it from emitted electrons, and high density plasma sheaths with mass velocity.

A. Note on V_{em} and V_c

In Reference 1, Equation 3 for the current flow at the emitter is written as

$$I = I_{th} + I_{iem} = I_{eem} \exp\left(-\frac{eV_{em}}{kT_{e1}}\right) \text{ for negative } V_{em} \text{ (zero plasma potential)} \quad (A-1)$$

and

$$I = I_{th} \exp\left(-\frac{eV_{em}}{kT_{eem}}\right) = I_{eem} \text{ for positive } V_{em} \quad (A-2)$$

From Equation A-1, solving for V_{em}

$$V_{em} = -\frac{kT_{e1}}{e} \ln\left[\frac{I_{eem}}{I_{th} + I_{iem} - I}\right] \quad (A-3)$$

$$= -\frac{kT_{e1}}{e} \ln\left[\frac{n_{e1}e}{J_{th} + J_{iem} - J} \sqrt{\frac{kT_{e1}}{2\pi m_e}}\right]$$

Similarly at the collector, for $V_c < 0$

$$V_c = -\frac{kT_{e2}}{e} \ln\left[\frac{n_{e2}e}{J + J_{ie}} \sqrt{\frac{kT_{e2}}{2\pi m_e}}\right] \quad (A-4)$$

Taking into account the resistive drop in the cell, the net voltage of the generator becomes

$$V_{net} = V_{em} + V_c + \phi_c - \phi_e - IR \quad (A-5)$$

It is seen from this equation that for $\phi_c = \phi_e = 0$, the barrier potentials at the cathode and the anode are of first importance. Looking at Equations A-3 and A-4 above, it becomes obvious that for $T_{e2} > T_{e1}$, V_c will decrease at least proportionally to a decrease in T_{e1} . Actually, the decrease in V_c is proportional to $T_{e2} \ln n_{e2}$. For $J = 0$ for example, $T_{e2} = 9000^\circ\text{K}$ ($T_{e2} = 12,000^\circ\text{K}$) in argon, $V_c(9000) \approx 0.57 V_c(12,000)$. One should also note that J_{rem} is in general larger than J_{ic} by a factor proportional to collector-to-emitter ratio $1/\beta$.

The equivalent expression to Equation 1, with $T_{e1} > T_{e2}$ is

$$V = V_{T_1} \ln \left[\frac{1 + \gamma/\delta - 1}{\gamma/\delta\beta + 1} \right]^{1/T_r} + \phi_c - \phi_e - IR \quad (\text{A-6})$$

where $T_r = T_{e1}/T_{e2}$, and subscript 1 and 2 refer to plasma conditions at emitter and collector respectively.

B. Thermoelectric Effects in a Joule-Heated Plasma

N. Ryan (Reference 8) and L. S. Hall (Reference 9) have analyzed the thermoelectric effects in fully ionized joule-heated plasmas. It is a straightforward method to extend the analysis to the case of partially ionized gases. Assume $n_1 = n_e = n$ and n_a neutrals. Neglecting inertia terms the equation of motion for electrons, according to Cowling (Reference 10), leads to,

$$0 = -\nabla p_e + ne\vec{E} + nm_e \vec{v} \tau^{-1} + nm_e \left\{ \vec{v} \cdot \vec{v}_1 (1 + n/n_a) \right\} \tau_e^{-1} \quad (\text{B-1})$$

and for ions

$$(1-f) \rho \frac{d\vec{v}_1}{dt} = -\nabla p_1 + ne\vec{E} + \frac{m_e}{\tau_e} \vec{j} + \frac{m_1}{2e\tau_1} \vec{j}_1 f^{-1} \quad (\text{B-2})$$

where

$$f^{-1} = 1 + n/n_a$$

$$\vec{j} = ne\vec{v}, \quad \vec{j}_1 = nev_1$$

\vec{v} = the velocity of the mass as a whole

τ = time between successive collisions

The rest of the notation is conventional.

Adding Equations B-1 and B-2,

$$f \nabla p_e = \frac{m_e}{e \tau} \vec{j} + j_1 f^{-1} \left[\frac{m_e}{e \tau_e} + \frac{m_1}{2e \tau_1} \right],$$

substituting for j_1 in the electron equation, yields

$$neE + \left[1 - f \frac{\frac{m_e}{e \tau_e}}{\frac{m_e}{e \tau_e} + \frac{m_1}{2e \tau_1}} \right] \nabla p_e = \left[\frac{m_e}{e \tau_e} + \frac{\frac{m_1 m_e}{2e \tau_1 + e \tau_e}}{\frac{m_e}{e \tau_e} + \frac{m_1}{2e \tau_1}} \right] \vec{j}. \quad (B-3)$$

For $m_e/m_1 \ll 1$ Equation B-3 simplifies to

$$neE + \nabla p_e = \frac{m_e}{e \tau} \vec{j} \quad (B-4)$$

From here on we follow Rynn (Reference 8) and write the current and energy equations for one dimensional motion

$$\left. \begin{aligned} j &= -\sigma E + b\sigma \frac{d\theta}{dx} \\ Q &= c\sigma\theta E - d\sigma\theta \frac{d\theta}{dx} \\ \frac{dQ}{dx} &= -jE + \frac{5}{2} j \frac{d\theta}{dx} \end{aligned} \right\} \quad (B-5)$$

where $\theta = \frac{kT}{e}$ and the rest of the terms are identical to those of Reference 8, except for the additional term on the right of the third equation. Integrating this equation and setting $\psi = 0$, $\theta = \theta_0 \left(E + \frac{d\psi}{dx} \right) \frac{d\theta}{dx} = 0$,

$$\begin{aligned} Q &= -j(\psi + \theta_0 e^{\psi} - f\theta) \\ &= -j(4 - f\theta) \quad f = \frac{5}{2} \end{aligned}$$

Substituting these values in the first two equations of B-5 and introducing the new variable $\eta = \psi/\theta$, the following equation is obtained

$$\frac{d\theta}{\theta} = \frac{c - (\eta - f)}{\eta(\eta - f) - [c\eta + b(\eta - f)] + d} d\eta \quad (B-6)$$

Equation B-6 differs from that of Rynn only by the additional constant $1 - \alpha/2$. The solution of this equation is given as a quadrature in References 8 and 9 where the thermoelectric effects are shown to skew the electron temperature distribution towards the cathode. Lewis and Reitz (Reference 11) calculate the increase in electron temperature by joule heating and for 50 amp/cm^2 current levels, 0.06 mm Hg electron pressures and 3000°K initial temperature, obtain a value of $T_e = 6000^\circ\text{K}$. For $j = 5 \text{ amp/cm}^2$ encountered in the present ASP generators, the rise of these emitter electron temperatures is not more than a few hundred degrees, and for arc jet plasma temperatures, $T_e \approx 12,000^\circ\text{K}$, it is negligible and actually is camouflaged by collisions with the energetic plasma electrons.

C. High Density Plasma Sheaths with Mass Motion

With gas densities up to 0.1 atmosphere, neutral gas atoms mean free paths $\lambda \ll R$, (R model body dimension) and mass velocities $v \approx 15,000 \text{ ft/sec}$, it is imperative for one to take a more careful look at the plasma barriers and ion arrival rates with increased mass velocities, $v_p \approx v$, at the electrodes ($v_p \ll v$). In collisionless plasmas, an initial velocity of 600 m/sec in the ions (see Reference 1, Equation B-11) will cause a 25 percent reduction in electron emission. However, in diffusion-controlled plasmas, such a direct estimate is difficult to make and an entirely different approach is necessary. Only a general outline will be given here, with details left for a future work.

The governing equations of motion for ion and electron diffusion in a slightly ionized gas of known flow characteristics are

$$q \cdot \nabla n_i + \nabla \cdot \Gamma_i = 0 \quad (C-1)$$

$$q \cdot \nabla n_e + \nabla \cdot \Gamma_e = 0$$

where

$$\Gamma_i = -D_i \nabla n_i - eZ\mu_i n_i \nabla \phi$$

$$\Gamma_e = -D_e \nabla n_e + e\mu_e n_e \nabla \phi$$

and Poisson's equation

$$\nabla^2 \phi = -4\pi e (Zn_i - n_e) \quad (C-2)$$

where D = diffusion coefficient, μ = mobility, ϕ = potential

Following the notations of Lamb (Reference 12), these three equations can be nondimensionalized to yield

$$\begin{aligned} \epsilon \frac{\partial^2}{\partial \eta^2} \psi &= N_1 - N_e \\ R(V + \nabla N_1) + \nabla \cdot \gamma_1 &= 0 \\ \frac{D}{\epsilon D_e} R(V + \nabla N_e) + \nabla \cdot \gamma_e &= 0 \end{aligned} \quad (C-3)$$

where

$$\begin{aligned} R &= \frac{1}{D_1} \frac{\partial}{\partial \eta} = \epsilon \frac{1}{Z T_1} \frac{\partial}{\partial x}, \quad N_{e,1} = n_{e,1} / n_0, \quad \psi = -e \phi / k T_1 \\ \epsilon &= h_1 / L, \quad h_1 = \text{Debye length} \end{aligned}$$

The analysis is then divided into two regions, (1) The ambipolar diffusion region and the sheath region with matching boundary conditions at the interface, (2) The sheath solution leads to the third order nonlinear equation

$$\epsilon \frac{d^3 \psi}{dt^3} = (\epsilon + 1) \frac{d\psi}{dt} \frac{d^2 \psi}{dt^2} + \frac{1}{2} \frac{d\psi}{dt} \left[\left(\frac{d\psi}{dt} \right)^2 + 2(1 + \epsilon)t \right] = (1 + \epsilon)N \quad (C-4)$$

where t is sheath coordinate, proportional to the normal coordinate to the surface, and $N = (n + \nabla \psi_0) / \sqrt{R}$ is determined from the diffusion solution,

For $T_e = T_1$, $\epsilon = 1$, Equation C-4 simplifies to

$$\frac{d^3 \psi}{dt^3} = \frac{1}{2} \frac{d\psi}{dt} \left[\left(\frac{d\psi}{dt} \right)^2 + 4t \right] = 2N \quad (C-5)$$

subject to boundary conditions

$$\frac{d^2 \psi}{dt^2} = 1 \text{ at } t = 0$$

where $F(\psi)$ is a function of the potential distribution in the sheath determined from interaction (collision) between the emitted electrons and the plasma electrons

$$\left(\frac{d\psi}{dt}\right)^2 = 4\psi_0 + 2\psi_{th} F(\psi)$$

and

$$\frac{d\psi}{dt}(\psi = 0) = \sqrt{\psi_0}$$

For a floating potential, $\psi = \psi_0 = 0$, from Equation C-1 and C-2 one can show that $\Gamma_+ = \frac{1}{4} \ln \left(\frac{3\beta}{4\beta+1} \right)$ or, the ion current and consequently electron emission is reduced by a factor of the Knudsen number at the wall. A more realistic situation for ASP would be to consider a collision dominated ambipolar region and a free fall sheath region with boundary condition (a) replaced by

$$\frac{d^2\psi}{dt^2} = \Gamma_{th} \exp(\psi/\delta) \left\{ 1 + \operatorname{erf} \sqrt{\psi/\delta} \right\}, \quad \delta = T_e/T_{em}$$

Analyses along these lines are presently under way, and results will be forthcoming in a separate report.

LIST OF REFERENCES

1. Touryan, K. J., The Hypersonic Plasma Converter: I, SC-4960(RR), Sandia Laboratory, Albuquerque, January 1964.
2. Touryan, K. J., A Hypersonic Plasma Power Generator, AIAA, 1st Annual Meeting, Washington, D. C., preprint 64-449, June 1964.
3. Byatt, W. J., Weinstein, G. E., Hypersonic Plasma Thermionic Generator, University of New Mexico Tech. Report EE-108, June 1964.
4. Weymouth, J. E., "Electrical Energy From High-Temperature Plasmas," J. E. E. Journal, pp. 380-383, August 1962.
5. Lewis, H. W., and Rentz, J. R., "Efficiency of the Plasma Thermocouple," J. Appl. Phys., Vol. 31, No. 4, April 1960.
6. Lubeck, P. T., Operation Characteristics of the Sandia 160 KW Plasma Arc Tunnel, (to be published as Sandia Corporation Research Report).
7. Shipley, K. L., Spectrographic Analysis of Plasmajets Progress Report II, SC-4776(RR), Sandia Laboratory, Albuquerque, March 1963.
8. Rynn, N., "Macroscopic Transport Properties of a Fully Ionized Alkali-Metal Plasma," Phys. of Fluids, Vol. 7, No. 2, February 1964.
9. Hall, L. S., "Thermoelectric Effects in a Joule-Heated Plasma," Phys. of Fluids, Vol. 7, No. 3, March 1964.
10. Cowling, T. G., "Magnetohydrodynamic", Interscience Publishers, Inc., New York, No. 4, 1957.
11. Lewis, H. W., Rentz, J. R., "Efficiency of the Plasma Thermocouple," J. Appl. Phys., Vol. 31, No. 4, April 1960.
12. Lamb, H. W., "A General Theory for the Flow of Weakly Ionized Gases," AIAA Journal, Vol. 2, No. 2, February 1964.

DISTRIBUTION:

AFCE Technical Library, Washington, D. C. (3)
Aero-Thermodynamics Standard Distribution (182)
DHE (325)
OFS (75)
Comdr. AFSWC, Attn: Chief Mail and Message Div., KAFB, N. Mex. 87177 (Code 1438) (13)
FC/DASA (53)
Theodore Cotter, N-5, LASL
Prof. W. W. Grannemann
Department of Electrical Engineering
University of New Mexico
Albuquerque, New Mexico
Col. D. Middlekauff
Ballistic Missile Re-entry Systems
Ballistic Systems Division (AFSC)
Norton Air Force Base, California
Ellis L. Foster, Jr.
Advanced Materials Technology
Battelle Memorial Institute
505 King Avenue
Columbus 1, Ohio (3)
C. F. Bild, 1100
L. A. Hopkins, 1300
J. H. Findlay, 1400
W. A. Gardner, 1500
L. D. Smith, 1600
C. S. Selvage, 1631
T. B. Heaphy, 3411
L. D. Patterson, 3411-1
For: H. F. Carroll, USMEC
Bertha R. Allen, 3421
Mavis G. Randle, 3428-1, Bldg. 836
Mavis G. Randle, 3428-1, Bldg. 880
R. S. Claassen, 5100
O. M. Stuetzer, 5140
J. R. Banister, 5153
T. B. Cook, Jr., 5400
R. M. Betz, 6010
L. E. Hollingsworth, 7200
D. B. Shuster, 7400
V. L. Blake, Jr., 7410
A. Y. Pope, 7420
H. R. Vaughn, 7421 (5)
K. J. Touryan, 7421-1 (5)
R. C. Maydew, 7422
W. H. Curry, 7424
M. L. Kramm, 7430
L. Gutierrez, 8100
D. R. Cotter, 9100
R. C. Smelich, 3427-3 (10)